Schmidt, A. et al. (2020) Probing the core of the strong nuclear interaction. *Nature*, 578(7796), pp. 540-544. (doi: 10.1038/s41586-020-2021-6)

Probing the core of the strong nuclear interaction

A. Schmidt et al. (CLAS Collaboration)

The strong nuclear interaction between nucleons (protons and neutrons) is the effective force that holds the atomic nucleus together. This interaction stems from fundamental interactions between quarks and gluons (the constituents of nucleons) that are described by the equations of Quantum Chromodynamics (QCD). However, as these equations cannot be solved directly, physicists resort to describing nuclear interactions using effective models that are well constrained at typical inter-nucleon distances in nuclei [1-5] but not at shorter distances. This limits our current ability to describe high-density nuclear matter such as in the cores of neutron stars [6]. Here we use high-energy electron scattering measurements that isolate nucleon pairs in short-distance, high-momentum configurations [7-9] to test nucleon-nucleon (*NN*) interactions at previously unreachable short distances, corresponding to relative momenta above 400 MeV/*c*. As the relative momentum between two nucleons increases and their separation thereby decreases, we observe a transition from a spin-dependent tensor-force to a predominantly spin-independent scalar-force. Using a nonrelativistic potential approach, we find that of the two main types of modern *NN* interactions, Chiral Effective Field Theory (χEFT) interactions provide a good description of our data up to their cutoff scale, while the phenomenological AV18 interaction describe our data well over the entire measured range of 400 – 1000 MeV/*c*. Accounting for relativistic effects using a Light-Cone formalism extends the agreement between the χEFT interactions prediction and the data over the entire range, similar to the phenomenological interactions. These results demonstrate the power of using such measurements to study the nuclear interaction at short-distances and also support the use of point-like nucleons with two- and three-body effective interactions to describe nuclear systems up to densities several times higher than the central density of atomic nuclei.

The primary experimental data used to constrain models of the *NN* interaction come from *NN* elastic scattering phase-shifts [1-5], measured up until the early 1990s. While this approach is highly precise, its scope of applicability is limited to relative momenta below the pion production threshold, approximately 400 MeV/*c*.

We study the *NN* interaction at nucleon momenta between 400 and 1000 MeV/*c* by measuring properties of Short-Ranged Correlations (SRCs), which are naturally occurring local density fluctuations, caused by pairs of strongly interacting nucleons at short distances [7-9]. To this end, we measured large momentum-transfer quasi-elastic (QE) electron scattering from a range of nuclei, studying events with either one or two protons detected in coincidence with the scattered electron (written as A(*e,e'p*) and A(*e,e'pp*), respectively), see Fig. 1. These measurements are done in kinematical conditions dominated by the hard breakup of SRC pairs, see details below. Models of the *NN* interaction are then tested by comparing the measured SRC breakup data to calculations using the Generalized Contact Formalism (GCF), an approach in which the structure of the SRC pair is factorized from the structure of the rest of the nucleus [10-12].

We find our data to be sensitive to the properties of the interaction between nucleons in SRC pairs, even up to 1000 MeV/*c*, i.e., four times the typical nuclear Fermi momentum k_F. Its comparisons with various GCF-based calculations show good agreement, thereby validating the GCF assumptions and the more-general use of point-like nucleons with effective interactions for modeling the nuclear interaction, even at very high-momenta where the *NN* interaction is not directly constrained and where experiments suggest significant modification of the internal structure of bound nucleons [7, 13].

These conclusions are based on the following observations, that are discussed in detail below: (1) the extracted fraction of pp-SRC pairs increases linearly from nucleon momenta of about 400 to about 650 MeV/*c*, and then appears to level off. This indicates a transition from tensor to scalar *NN* interactions at high-momenta, (2) The extracted initial nucleon momentum and energy distributions, as well as their correlation (i.e., the nuclear spectral function), are remarkably well described by the non-relativistic GCF model using the phenomenological AV18 *NN* interaction [4] up to momenta of 1000 MeV/*c*. (3) Using local χEFT *NN* interactions [5] also describe the data well, but only up to ~ 600 MeV/*c*, which corresponds to the χEFT 'cutoff'. This shows the importance of higher order corrections above this cutoff, and (4) Using a light-cone formalism to account for relativistic effects in the nuclear wave function has little impact on the phenomenological calculations but dramatically improves the agreement between the data and χEFT calculations, significantly reducing the importance of higher order corrections.

Our studies are done within the single-photon exchange approximation [7–9, 14–18], where electrons scatter from

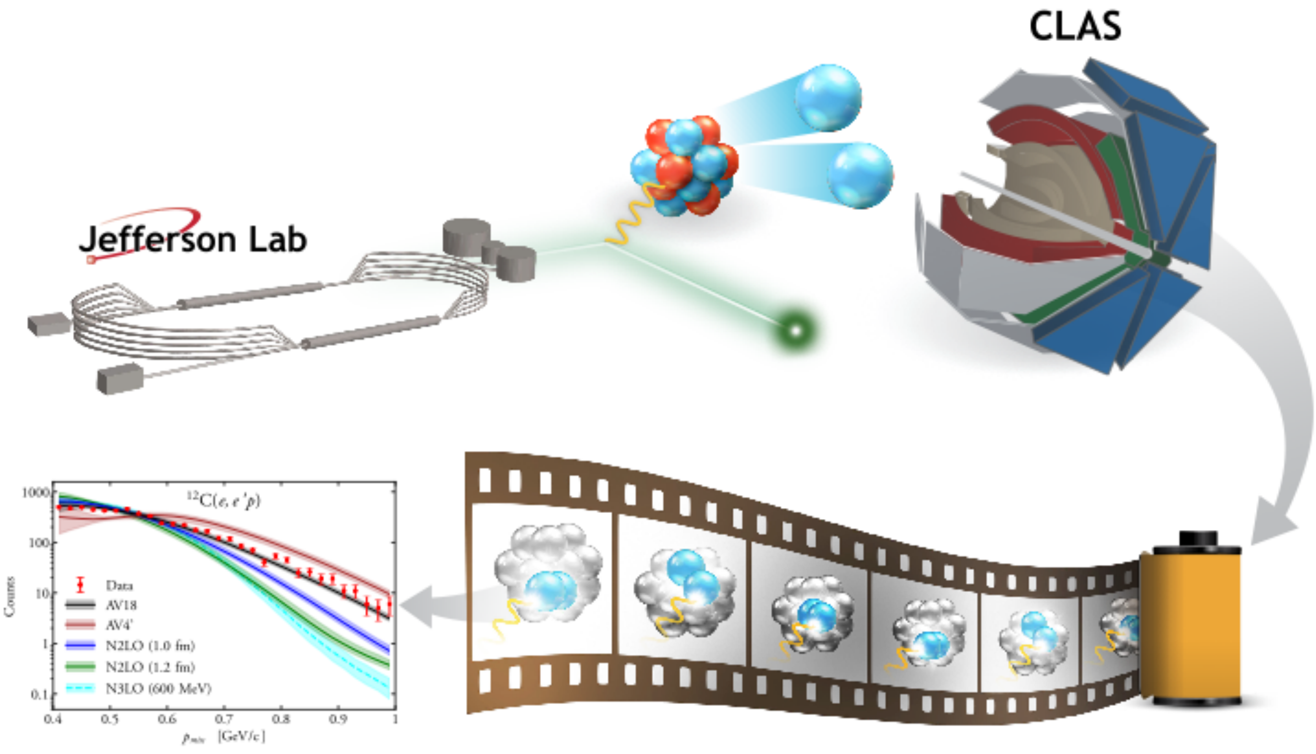

Fig. 1 | Using Electron Scattering Measurements to Constrain the Nuclear Interaction. (a) 5 Giga Electron-Volt (GeV) electrons from the Jefferson Lab accelerator impinge on nuclei and break apart short-range correlated (SRC) nucleon pairs. The CLAS spectrometer is used to detect the scattered electron and knockout protons which allows reconstructing their initial state inside the nucleus. (b) By combining many such measurements the distribution of such pairs inside the nucleus is assembled and compared to theoretical calculations using different models of the strong nuclear interaction.

the nucleus by transferring a virtual photon carrying momentum $\boldsymbol{q}$ and energy ω. In the high-resolution one-body view of QE scattering at large momentum transfer, the virtual photon is absorbed by a single off-shell nucleon with initial energy ϵ_i and momentum $\boldsymbol{p}_i$. If the nucleon does not re-interact as it leaves the nucleus, it will emerge with momentum $\boldsymbol{p}_N = \boldsymbol{p}_i + \boldsymbol{q}$ and energy $\epsilon_N = \omega + \epsilon_i$. Outgoing nucleon rescattering from other nucleons can change the detected momentum and energy. However, we can approximate the initial momentum and energy of that nucleon as the measured missing momentum $\boldsymbol{p}_{miss} \equiv \boldsymbol{p}_N - \boldsymbol{q} \approx \boldsymbol{p}_i$ and the missing energy $E_{miss} \equiv \omega - T_N \approx m_N - \epsilon_i$ (where $T_N = \epsilon_N - m_N$ is the detected nucleon kinetic energy). See Methods for discussion of nucleon rescattering effects.

Without SRC pairing, almost all nucleons in atomic nuclei occupy momentum states up to the nuclear Fermi momentum k_F (~ 250 MeV/*c*). However, nucleons in SRC pairs move with momenta greater than k_F [7, 8]. When $p_{miss} > k_F$, the knockout nucleon should therefore predominantly be part of an SRC pair and the knockout of one nucleon from the pair should be accompanied by the simultaneous emission of a second (recoil) nucleon with momentum $\boldsymbol{p}_{recoil} \approx -\boldsymbol{p}_i$ [14 - 18], see Extended Data Fig. 2.

Previous A(*e,e'p*) studies observed that non-QE reaction mechanisms can lead to high p_{miss} events that are not due to the knockout of nucleons from SRC pairs. To minimize such contributions, our measurement was performed at kinematics where non-SRC contributions were shown to be suppressed [8, 19–21], namely: $Q^2 \equiv \boldsymbol{q}^2 - \omega^2 \gtrsim 1.5$ (GeV/c^2)^2 and $x_B \equiv Q^2/2\mathrm{m_N}\omega \geq 1.2$ (where $\mathrm{m_N}$ is the nucleon mass) so that $\boldsymbol{p}_{miss}$ was almost anti-parallel to $\boldsymbol{q}$ and Q^2 grows with $\boldsymbol{p}_{miss}$. See Methods for details.

Previous measurements of A(*e,e'pN*) reactions off ^{4}He and ^{12}C, performed at these kinematics, have shown that proton-neutron (*pn*) SRC pairs predominate over proton-proton (*pp*) SRC pairs for $300 < p_{miss} < 600$ MeV/*c* by a factor of almost 20 [14-18]. This is due to a minimum in the spin-0 *pp* pair momentum distribution and indicates the dominance of the tensor part of the nuclear interaction in that momentum range; it operates on spin-1 pairs and therefore favors *pn* over *pp* SRC pairs (see Extended Data Fig. 1) [7, 8, 19]. At higher missing-momentum, the interaction is expected to be predominantly scalar, as the repulsive core of the *NN* interaction becomes dominant. This transition should lead to an increased fraction of *pp*-SRC pairs [15].

Here we extend these studies by measuring the A(*e,e'p*) and A(*e,e'pp*) reactions for $400 \leq p_{miss} \leq 1000$ MeV/*c* for C, Al, Fe and Pb nuclei. The measurements were done

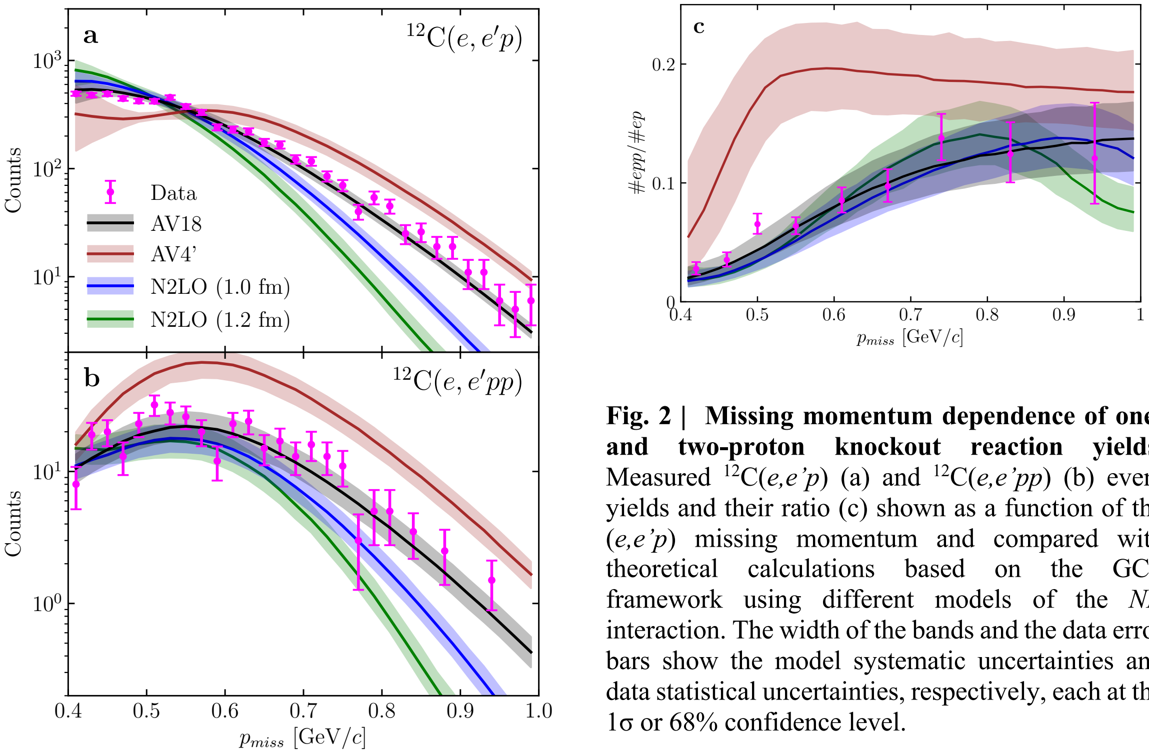

Fig. 2 | Missing momentum dependence of one- and two-proton knockout reaction yields. Measured ^{12}C(*e,e'p*) (a) and ^{12}C(*e,e'pp*) (b) event yields and their ratio (c) shown as a function of the (*e,e'p*) missing momentum and compared with theoretical calculations based on the GCF framework using different models of the *NN* interaction. The width of the bands and the data error bars show the model systematic uncertainties and data statistical uncertainties, respectively, each at the 1σ or 68% confidence level.

at the Thomas Jefferson National Accelerator Facility using a 5.01 GeV electron beam. The CEBAF Large Acceptance Spectrometer (CLAS) [22] was used to detect and identify the scattered electron and knockout protons and reconstruct their momenta, see Fig. 1.

We selected (*e,e'p*) events by considering all measured events with a scattered electron with $x_B \geq 1.2$ and a "leading" proton detected within a narrow cone of 25° around $\boldsymbol{q}$, carrying at least 60% of the transferred momentum ($p_N/q > 0.6$), and resulting in $400 < p_{miss} < 1000$ MeV/*c*. (*e,e'pp*) events are a subset of (*e,e'p*) events where a second, "recoil", proton was detected with momentum greater than 350 MeV/*c*. Due to the large momentum transfer, which grows with $\boldsymbol{p}_{miss}$, the recoil proton measured in (*e,e'pp*) events has significantly smaller momenta and a much wider angular distribution than the high-momentum leading proton. See Extended Data Figs. 3–6 for selected kinematical distributions of the measured (*e,e'p*) and (*e,e'pp*) events.

To quantitatively relate observations to the underlying nuclear interaction, we need to calculate the nucleon knockout cross section starting directly from the *NN* interaction.

At the high-Q^2 kinematics of our measurement the differential A(*e,e'p*) nucleon knockout cross sections can be approximately factorized as [23, 24]:

Eq. 1

$$\frac{d^6\sigma}{d\Omega_{k'}\,d\epsilon'_k\,d\Omega_{p_N}\,d\epsilon_N} = p_N\epsilon_N \cdot \sigma_{ep} \cdot S(\boldsymbol{p}_i, \epsilon_i),$$

where $\boldsymbol{k}'$ and ϵ'_k are the final electron momentum and energy, σ_{ep} is the off-shell electron-nucleon cross section [24] and $S(\boldsymbol{p}_i, \epsilon_i)$ is the nuclear spectral function that defines the probability for finding a nucleon in the nucleus with momentum $\boldsymbol{p}_i$ and energy ϵ_i [12]. Different models of the nuclear interaction can produce different spectral functions, making the measured cross sections sensitive to the nuclear interaction model.

The two-nucleon knockout cross section can be factorized similarly to Eq. (1) by replacing the single-nucleon spectral function with the two-nucleon decay function that defines the probability of finding nucleons with momenta $\boldsymbol{p}_i$ and $\boldsymbol{p}_{recoil}$ such that the A-1 system has energy E_r [9, 17, 19]. See Methods for details.

Ab-initio many-body calculations of the nuclear spectral and decay functions are currently computationally unfeasible [1]. However, for the specific case of interacting with SRC pairs (i.e. $p_i \approx p_{miss} > k_F$), we can effectively approximate these functions using the GCF [10 - 12] which assumes that at very high momenta, the nuclear wave-function can be described as consisting of an SRC pair and a residual A-2 system.

Therefore, in the GCF, the high-momentum proton spectral function of Eq. 1 is approximated by a sum over *pp* and *pn* SRC pairs, which allows calculating (*e,e'p*) and (*e,e'pp*) cross sections using different nuclear interaction models as input [12, 18] (see Methods for details). Here we consider two commonly used models: the phenomenological AV18 [4] and the Chiral EFT-based local N2LO [5] interactions, as well as the simplified, tensor-less, AV4' interaction. We used the N2LO interaction with two "cutoffs": 1.0 and 1.2 fm. The latter makes the potential tractable for many-body nuclear calculations by smoothing out shorter-distance structure (and reducing high-momentum strength).

The GCF calculation requires three additional input parameters: (a) the relative abundance of spin-1 (i.e. only *pn*-SRCs) to spin-0 (i.e. *pp*-, *nn*- and *pn*-SRCs) SRC pairs, (b) the width of the center-of-mass (CM) momentum distribution of SRC pairs and (c) the average excitation energy of the residual A-2 system after the pair knockout, E^*_{A-2}. For the aforementioned interactions (a) was extracted from ab-initio many-body calculations of ^{12}C [11, 25] and (b) was extracted from data [26], leaving E^*_{A-2} as the only unconstrained parameter.

To determine the systematic uncertainty of the GCF cross-section calculation, we repeated it many times, varying the input parameters each time and using the spread in the resulting calculations as a measure of the calculation uncertainty. For example, E^*_{A-2} was varied between 0 and 30 MeV, corresponding to knockout of loosely and tightly bound nucleons, respectively. See Methods for additional details.

We compared the GCF cross sections to experimental data using Monte Carlo integration, randomly generating A(*e,e'pN*) events (assuming the reaction diagram shown in Extended Data Fig. 2) and weighting each by the calculated GCF cross section. Electron radiative effects were included via a peaking approximation where the radiated photon is emitted in the direction of either the incoming or outgoing electron. Interaction effects such as final state interactions (FSI) and single-charge exchange (SCX) of the outgoing nucleons [8, 20, 21, 27 - 29] were accounted for using the Glauber calculations of Ref. [20], which agree well with experimental data [27 - 29]. As these effects are model-dependent, we chose to include them in the calculated cross sections, leaving the data fully model independent.

We further included detector acceptance and resolution effects through a simulation of the detector by smearing the momentum of each simulated particle based on the CLAS momentum reconstruction resolution and re-weighting events according to the product of the detection efficiencies for each detected particle. Lastly, we discarded all simulated events that did not pass the event selection cuts that were applied to the data. See Methods for details.

The resulting calculated ^{12}C(*e,e'pp*) and ^{12}C(*e,e'p*) yields for the two different *NN* interactions are shown in Fig. 2 (a) and (b) as a function of p_{miss}. The calculations are compared with the data and normalized to the integrated number of measured (*e,e'p*) events. The phenomenological AV18 interaction describes the measured p_{miss} distribution over the entire measured missing-momentum range. The χEFT N2LO interactions describe the data well up to about 600 - 700 MeV/*c*, consistent with their cutoffs. The simplified AV4' interaction, as expected, does not describe the momentum distributions well.

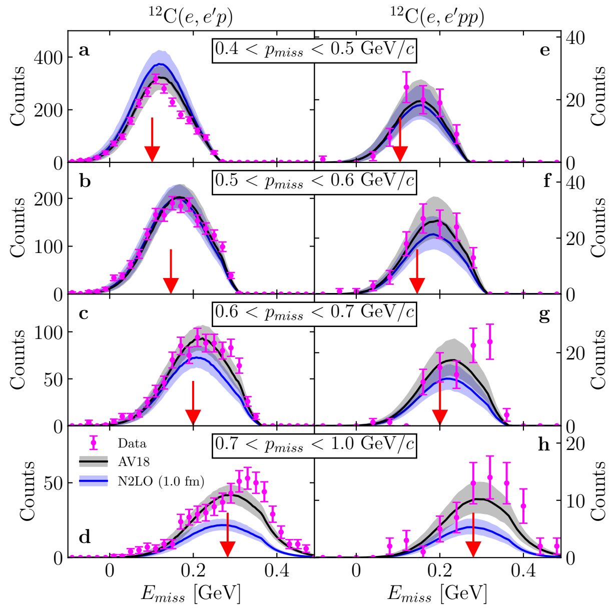

Fig. 3 | Nuclear spectral function at high momentum. Measured ^{12}C(*e,e'p*) (a-d) and ^{12}C(*e,e'pp*) (e-h) event yields shown as a function of E_{miss} for different bins in (*e,e'p*) p_{miss}. The data are compared with theoretical calculations based on the GCF framework, using different models of the *NN* interaction. The arrows mark the expected energy for a stationary pair with relative momentum that equals the mean momentum of each missing-momentum bin (see Methods). The width of the bands and the data error bars show the model systematic uncertainties and data statistical uncertainties, respectively, each at the 1σ or 68% confidence level.

Figure 2 (c) shows the measured ^{12}C(*e,e'pp*) / ^{12}C(*e,e'p*) event yield ratio as a function of p_{miss}, which increases linearly from 400 to about 650 MeV/*c* and then appears to flatten out (see Extended Data Fig. 7 for similar behavior observed for Al, Fe and Pb). The observed increase in this ratio, i.e., the fraction of (*e,e'p*) events with a recoil proton, is qualitatively consistent with the overall trend expected by a transition from a predominantly tensor to a predominantly scalar interaction at high p_{miss}.

This is supported by the observation that the fully-scalar AV4' interaction (i.e., which lacks the tensor force) agrees with data at the scalar-dominated high-momentum region but fails at tensor-dominated low-momentum region. In addition, we see that the data agrees with the AV18 and N2LO based GCF calculations. At high-momenta, these calculations predict a *pp*-SRC pair fraction of ~1/3, which is equal to the scalar limit one obtains by simple pair counting, see Methods and Extended Data Fig. 12 for details.

We also observe that the effect of the χEFT interaction cutoff largely cancels in the ^{12}C(*e,e'pp*) / ^{12}C(*e,e'p*) yield ratio leading to agreement with both the AV18 predictions and the data.

Next, we studied the nuclear spectral function $S(p_i, \epsilon_i)$ by examining the correlation between the missing energy and missing momentum of the ^{12}C(*e,e'pp*) and ^{12}C(*e,e'p*) reactions (Fig. 3). The average value of E_{miss} increases with p_{miss}, peaking at the expected value for the breakup of an SRC pair at rest, marked by a red arrow in Fig. 3. This supports our interpretation of the measured process being dominated by interacting with an SRC pair with the A-2 residual system being a spectator [30].

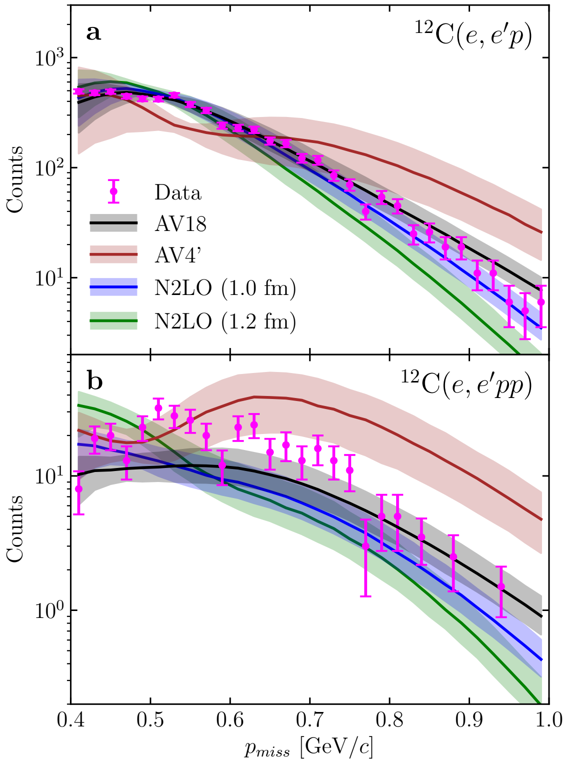

Fig. 4 | Relativistic effects in missing momentum dependence of one- and two-proton knockout reaction yields. Same data as shown in Fig. 2 (a) and (b) (i.e. measured ^{12}C(*e,e'p*) (a) and ^{12}C(*e,e'pp*) (b) event yields shown as a function of the (*e,e'p*) missing momentum), but compared with theoretical calculations based on the light-cone relativistic version of the GCF using different models of the *NN* interaction. The width of the bands and the data error bars show the model systematic uncertainties and data statistical uncertainties, respectively, each at the 1σ or 68% confidence level.

The GCF calculations follow the same trend of the data. However, while the AV18 interaction agrees with the data over the entire E_{miss} and p_{miss} range, the chiral interaction underpredicts the yield at high p_{miss} due to its cutoff.

Extended Data Figs. 4 – 6 show good agreement between the data and GCF calculation for various other kinematical distributions.

Two additional tests were done to ensure the suppression of non-QE reaction mechanisms: (1) We compared the A(*e,e'p*) and A(*e,e'pp*) p_{miss} and E_{miss} distributions for nuclei from C to Pb and observed that they are identical within uncertainties and (2) we examined in detail the distribution of the kinematical variables that are most sensitive to non-QE reaction mechanisms, such as the angle between $\boldsymbol{p}_{miss}$ and $\boldsymbol{q}$ [8, 19, 21], to find that they are well described by the GCF-based simulation, see Extended Data Figs. 8 and 9 and Methods for details.

Lastly, due to the high initial-momenta of the measured protons, we assessed the possible impact of relativistic effects on the nuclear wave-function in the GCF spectral function. As fully relativistic nuclear potentials and wave-functions are currently unavailable, the introduction of relativistic effects can only be done in an approximate and model-dependent manner. Here we used the relativistic nuclear light cone (LC) formalism of [9], which was previously used for SRC studies using nucleon knockout reactions [17], see Methods for details.

Figure 4 shows relativistic LC calculations of the ^{12}C(*e,e'pp*) and ^{12}C(*e,e'p*) yields as a function of p_{miss}, along with the same data shown in Figs. 2a and 2b (see Extended Data Fig. 14 for the LC equivalent of Fig. 3). Comparing with the non-relativistic calculations of Fig. 2, we observe that relativistic corrections do not produce a large change in GCF calculations when using phenomenological potentials, but do significantly impact the χEFT-based calculations. This stems from the fact that, in kinematics of our measurement, the relativistic treatment reduces the effective relative momenta of the probed *NN* pairs compared to the non-relativistic case presented above. For the χEFT calculations, this change reduces the probed relative momenta back towards their effective cut-offs even at very high p_{miss}, resulting in much better agreement with the data. This suggests that a relativistic treatment could reduce the necessity of applying higher order corrections in χEFT calculations at large p_{miss}.

Thus, we conclude that the large momentum transfer electron scattering measurements reported here are both sensitive to the detailed characteristics of the *NN* interaction at high relative momenta and well-described by the theoretical calculations presented above. This is surprising, not only because the input *NN* interaction models were not directly fit to high-momentum data, but also because previous studies have indicated that the large spatial overlap and high-virtuality of nucleons in SRC pairs may change their internal quark-gluon sub-structure [7, 13]. The fact that GCF calculations reproduce our data over the entire measured $\epsilon_{miss}-p_{miss}$ range suggests that such modification does not significantly impact the effective modeling of the nuclear interaction.

Our results therefore provide strong support for the use of point-like nucleons with effective interactions for modeling both atomic nuclei and dense astrophysical systems such as neutron stars, whose outer core already exceeds nuclear saturation density.

The success of the framework presented here for studying the *NN* interaction also paves the way for future studies of the loosely constrained three-nucleon (i.e. *NNN*) interaction by extending the GCF to model forthcoming three-nucleon knockout measurements.

References:

[1] "Quantum Monte Carlo methods for nuclear physics", J. Carlson, S. Gandolfi, F. Pederiva, S. C. Pieper, R. Schiavilla, K. E. Schmidt, and R. B. Wiringa, Rev. Mod. Phys. **87**, 1067 (2015).

[2] "Modern theory of nuclear forces", E. Epelbaum, H.W. Hammer and U.G. Meißner, Rev. Mod. Phys. **81**, 1773 (2009).

[3] "The bonn meson-exchange model for the nucleon—nucleon interaction", R. Machleidt, K. Holinde, and C. Elster, Phys. Rept. **149**, 1 (1987).

[4] "Accurate nucleon-nucleon potential with charge-independence breaking", R. B. Wiringa, V. G. J. Stoks, and R. Schiavilla, Phys. Rev. C **51**, 38 (1995).

[5] "Quantum Monte Carlo Calculations with Chiral Effective Field Theory Interactions", A. Gezerlis, I. Tews, E. Epelbaum, S. Gandolfi, K. Hebeler, A. Nogga, and A. Schwenk, Phys. Rev. Lett. **111**, 032501 (2013).

[6] "Neutron Star Observations: Prognosis for Equation of State Constraints" J.M. Lattimer and M. Prakash, Phys. Rept. **442**, 109 (2007).

[7] "Nucleon-Nucleon Correlations, Short-lived Excitations, and the Quarks Within", O. Hen, G.A. Miller, E. Piasetzky, and L. B. Weinstein, Rev. Mod. Phys. **89**, 045002 (2017).

[8] "In-medium short-range dynamics of nucleons: Recent theoretical and experimental advances", C. Ciofi degli Atti, Phys. Rep. **590**, 1 (2015).

[9] "High-Energy Phenomena, Short Range Nuclear Structure and QCD", L. Frankfurt, and M. Strikman, Phys. Rep. **76**, 215 (1981).

[10] "Generalized nuclear contacts and momentum distributions", R. Weiss, B. Bazak, and N. Barnea, Phys. Rev. C **92**, 054311 (2015).

[11] "The Nuclear Contacts and Short-Range Correlations in Nuclei", R. Weiss, R. Cruz-Torres, N. Barnea, E. Piasetzky, and O. Hen, Phys. Lett. B **780**, 211 (2018).

[12] "Energy and momentum dependence of nuclear short-range correlations - Spectral function, exclusive scattering experiments and the contact formalism", R. Weiss, I. Korover, E. Piasetzky, O. Hen, and N. Barnea, Phys. Lett. B **791**, 242 (2019).

[13] "Modified Structure of Protons and Neutrons in Correlated Pairs", B. Schmookler et al. (CLAS Collaboration), Nature **566**, 354 (2019).

[14] "Probing Cold Dense Nuclear Matter", R. Subedi et al., Science **320**, 1476 (2008).

[15] "Approaching the nucleon-nucleon short-range repulsive core via the ^{4}He(*e,e'pN*) triple coincidence reaction", I. Korover et al., Phys. Rev. Lett. **113**, 022501 (2014).

[16] "Momentum Sharing in Imbalanced Fermi Systems", O. Hen et al. (CLAS Collaboration), Science **346**, 614 (2014).

[17] "Evidence for the strong dominance of proton-neutron correlations in nuclei", E. Piasetzky, M. Sargsian, L. Frankfurt, M. Strikman, and J.W. Watson, Phys. Rev. Lett. **97**, 162504 (2006).

[18] "Direct Observation of Proton-Neutron Short-Range Correlation Dominance in Heavy Nuclei", M. Duer et al. (CLAS Collaboration), Phys. Rev. Lett. **122**, 172502 (2019).

[19] "Recent observation of short-range nucleon correlations in nuclei and their implications for the structure of nuclei and neutron stars", L. Frankfurt, M. M. Sargsian, and M. Strikman, Int. J. Mod. Phys. A **23**, 2991 (2008).

[20] "Final-state interactions in two-nucleon knockout reactions", C. Colle, W. Cosyn, and J. Ryckebusch, Phys. Rev. C **93**, 034608 (2016).

[21] "Selected Topics in High Energy Semi-Exclusive Electro-Nuclear Reactions", M. M. Sargsian, Int. J. Mod. Phys. E **10**, 405 (2001).

[22] "The CEBAF large acceptance spectrometer (CLAS)", B. A. Mecking et al., Nucl. Inst. Meth. A **503**, 513 (2003).

[23] "Nucleon knockout by intermediate-energy electrons", J.J. Kelly, Adv. Nucl. Phys. **23**, 75 (1996).

[24] "Off-shell electron-nucleon cross sections: The impulse approximation", T. De Forest, Nucl. Phys. A **392**, 232 (1983).

[25] "Scale and Scheme Independence and Position-Momentum Equivalence of Nuclear Short-Range Correlations" R. Cruz-Torres, D. Lonardoni, R. Weiss, N. Barnea, D.W. Higinbotham, E. Piasetzky, A. Schmidt, L.B. Weinstein, R.B. Wiringa, and O. Hen, arXiv: 1907.03658 (2019).

[26] "Center of Mass Motion of Short-Range Correlated Nucleon Pairs studied via the A*(e,e'pp)* Reaction", E. O. Cohen et al. (CLAS Collaboration), Phys. Rev. Lett. **121**, 092501 (2018).
[27] "Measurement of Transparency Ratios for Protons from Short-Range Correlated Pairs", O. Hen et al. (CLAS Collaboration), Phys. Lett. B **722**, 63 (2013).
[28] "Measurement of Nuclear Transparency Ratios for Protons and Neutrons", M. Duer, et al. (CLAS Collaboration), Phys. Lett. B **797**, 134792 (2019).
[29] "Extracting the mass dependence and quantum numbers of short-range correlated pairs from A*(e,e'p)* and A*(e,e'pp)* scattering", C. Colle et al., Phys. Rev. C **92**, 024604 (2015).
[30] "Two nucleon correlations and the structure of the nucleon spectral function at high values of momentum and removal energy", C. Ciofi degli Atti, S. Simula, L.L. Frankfurt, and M.I. Strikman, Phys. Rev. C **44**, R7 (1991)

Methods:

CLAS Detector and Particle Identification:

CLAS was a 6-sector toroidal magnetic spectrometer [22]. Each sector was equipped with three layers of drift chambers, time-of-flight scintillation counters, Cerenkov counters, and electromagnetic calorimeters. The drift chambers and time-of-flight scintillation counters covered in-plane scattering angles from about 8° to 140°, while the Cerenkov counters and electromagnetic calorimeters covered about 8° to 45°. The 6 sectors collectively offered ≈80% out-of-plane angular coverage.

Charged particles interacted in the drift chambers, allowing reconstruction of their trajectories as they bent due to the influence of the toroidal magnetic field. The charge of charged particles (electrons and protons in this work) and their momenta were determined from their reconstructed trajectories. We consider only charged particle whose trajectories were reconstructed to originate in the location of the solid target foil, see [31] for details.

Electrons were distinguished from pions by requiring a large signal in the Cerenkov counters, as well as a large energy deposition in the Electromagnetic Calorimeters that is proportional to momentum. Protons were identified by requiring that their time-of-flight, measured by the scintillation counters, be within two standard deviations of the calculated time-of-flight based on the momentum reconstructed in the drift chambers, assuming the particle has the mass of a proton.

GCF Model:

The derivation of the GCF and its application for describing SRCs in nuclei are detailed in Refs. [10 - 12, 25, 32, 33]. It is applicable at missing momenta where SRC dominates [11]. Here we review its main characteristics that are relevant for this work.

The GCF is a generalization of the atomic contact formalism, successfully used to describe scale-separated, strongly interacting, two-component Fermi systems. It assumes that at very high momenta, the asymptotic nuclear many-body ground state wave function Ψ^A can be factorized into an SRC pair and a residual A-2 system as [10, 11]:

$$\text{Eq. 2} \qquad \Psi^A \xrightarrow{p_{12}\to\infty} \sum_{\alpha} \tilde{\varphi}^{\alpha}_{12}(\boldsymbol{p}_{12}) \tilde{A}^{\alpha}_{12}(\boldsymbol{P}_{12}, \{\boldsymbol{p}_k\}_{k\neq 1,2}),$$

where α denotes the SRC pair quantum numbers, $\tilde{\varphi}^{\alpha}_{12}(p_{12})$ are universal two-body functions of the relative momentum of the SRC pair $\boldsymbol{p}_{12} = (\boldsymbol{p}_1 - \boldsymbol{p}_2)/2$, and $\tilde{A}^{\alpha}_{12}$ describes the motion of the A-2 system with total pair CM motion, $\boldsymbol{P}_{12} = (\boldsymbol{p}_1 + \boldsymbol{p}_2)$. $\tilde{\varphi}^{\alpha}_{12}(p_{12})$ are normalized such that the integral over $|\tilde{\varphi}^{\alpha}_{12}(p_{12})|^2$ from k_F to infinity equals 1 [10, 11].

Under this approximation, the asymptotic high-momentum proton spectral function (Eq. 1) can be written as a sum over SRC pairs [12]:

$$\text{Eq. 3} \qquad S^p(p_{\mathrm{i}}, \epsilon_{\mathrm{i}}) = C^{s=1}_{pn} S^{s=1}_{pn}(p_{\mathrm{i}}, \epsilon_{\mathrm{i}}) + C^{s=0}_{pn} S^{s=0}_{pn}(p_{\mathrm{i}}, \epsilon_{\mathrm{i}}) + 2C^{s=0}_{pp} S^{s=0}_{pp}(p_{\mathrm{i}}, \epsilon_{\mathrm{i}}),$$

where C^{α}_{NN} are the nuclear contacts, which measure the probability to find a proton-proton (pp) pair or a proton-neutron (pn) pair with quantum numbers α close together. The functions $S^{\alpha}_{NN}(p_{\mathrm{i}}, \epsilon_{\mathrm{i}})$ are the individual contributions of these pairs to the total spectral function. The $s = 1$ state corresponds to the spin-one deuteron state, and $s = 0$ corresponds to the spin-zero s-wave state.

The single-pair spectral function $S^{\alpha}_{NN}(p_{\mathrm{i}}, \epsilon_{\mathrm{i}})$ is given by a convolution of its relative and CM motion:

$$\text{Eq. 4} \qquad S^{\alpha}_{NN}(p_{\mathrm{i}}, \epsilon_{\mathrm{i}}) = \frac{1}{4\pi} \int \frac{d\boldsymbol{p}_{recoil}}{(2\pi)^3} \delta\big(f(\boldsymbol{p}_{recoil})\big)\, \Theta\big(\boldsymbol{p}_{rel} - p^{min}_{rel}\big) |\tilde{\varphi}^{\alpha}_{NN}(\boldsymbol{p}_{rel})|^2 n^{\alpha}_{NN}(\boldsymbol{P}_{CM}),$$

and

$$\text{Eq. 5} \qquad f(\boldsymbol{p}_{recoil}) = \epsilon_{\mathrm{i}} + \epsilon_{\mathrm{recoil}} - m_A + \sqrt{P^2_{CM} + (m_{A-2} + E^*_{A-2})^2} \qquad ,$$

where $\boldsymbol{P}_{CM} \equiv \boldsymbol{p}_i + \boldsymbol{p}_{recoil}$, $\boldsymbol{p}_{rel} \equiv |\boldsymbol{p}_i - \boldsymbol{p}_{recoil}|/2$, $n_{NN}^{\alpha}(P_{CM})$ is the CM momentum distribution of the SRC pair given by $C_{NN}^{\alpha} n_{NN}^{\alpha}(\boldsymbol{P}_{CM}) = \langle \tilde{A}_{12}^{\alpha}(\boldsymbol{P}_{CM}) | \tilde{A}_{12}^{\alpha}(\boldsymbol{P}_{CM}) \rangle$, m_A and m_{A-2} are the ground state masses of the initial A and final A-2 nuclear systems, E_{A-2}^{*} is the excitation energy of the A-2 system, and $\epsilon_{\mathrm{recoil}}$ is the energy of the recoil nucleon. We assume that the pair CM momentum distribution is the same for all pairs: $n_{NN}^{\alpha}(\boldsymbol{P}_{CM}) = n_{CM}(\boldsymbol{P}_{CM})$. The step function $\Theta(\boldsymbol{p}_{rel} - p_{rel}^{min})$ ensured that we only integrate over pairs with large relative momentum, since the GCF models only SRC pairs that are expected to dominate above k_F. We note that while the universal functions used here are non-relativistic, we use relativistic expressions for the nucleon energies since the kinematics of the measured high-Q^2 processes is highly relativistic.

The integrand of Eq. 4 is called the two-body decay function $D_A(\boldsymbol{p}_i, \boldsymbol{p}_{recoil}, E_R)$, which represents the probability for a hard knockout of a nucleon with initial momentum $\boldsymbol{p}_i$, followed by an emission of a recoil nucleon with momentum $\boldsymbol{p}_{recoil}$ [9, 17, 18, 34]. E_R is the energy of the A−1 system, composed of the recoil nucleon and the residual A − 2 nucleus. Integrating the decay function over all recoil nucleon momenta ($\boldsymbol{p}_{recoil}$) yields the spectral function.

The GCF model, as presented above, requires four external inputs:

1. Nuclear contact values (C_{NN}^{α}): For the AV18, AV4', and N2LO we use nuclear contacts that were previously extracted from analyses of two-nucleon momentum distributions [11, 25], obtained from many-body Quantum Monte-Carlo calculations for C [35, 36]. Because we normalize the simulated event yields to the integrated number of *(e,e'p)* data events, our calculations are only sensitive to the relative values of the contacts.
2. Universal $\tilde{\varphi}_{12}^{\alpha}(p_{12})$ functions: These are taken as the solution of the two-body Schrodinger equation for nucleon pair 1-2 with quantum numbers α, see Refs. [10, 11] for details. $\tilde{\varphi}_{12}^{\alpha}(\boldsymbol{p}_{12})$ are nucleus-independent, but depend on the *NN* interaction model used in its calculation. In the case of the spin-1 ($s = 1$) quantum state this amounts to the deuteron wave-function shown in Extended Data Fig. 1 (a). For the spin-0 ($s = 0$) quantum state it is the zero-energy solution of the two-body *NN* system, see Extended Data Fig. 1 (b) for the pp channel.
3. SRC pairs center-of-mass momentum distributions: These distributions were studied both theoretically [37, 38] and experimentally [15, 26, 39, 40] and were found to be well described by a three-dimensional gaussian that is defined by its width. For the nuclei considered here, both measurements and theoretical calculations show this width to be about 150 ± 20 MeV/*c* [26].
4. Excitation energy of the A-2 system: Unlike the other inputs mentioned above, E_{A-2}^{*} was never measured before and can therefore take any value up to an order of the Fermi-energy (~ 30 MeV).

We note that as mentioned in main text, calculations of the nuclear spectral function are not feasible for generic nuclear systems. However, for the specific case of three-nucleon system and nuclear matter such calculations are feasible and their results agree with the model presented above [30].

GCF Event Generator, FSI, and SCX Corrections:

The GCF-based event generator used here simulates the reaction shown in Extended Data Fig. 2, in which an electron has a hard scattering from a nucleon in an SRC pair within a nucleus, causing both the struck nucleon and the correlated partner nucleon to be ejected from the nucleus. The generator generates particles over the full phase-space by sampling events randomly from the probability distribution:

$$\text{Eq. 6} \qquad P(Q^2, \mathrm{x_B}, \phi_{\mathrm{e}}, \boldsymbol{P}_{12}, \Omega_{\mathrm{p_2}}) = \frac{1}{\Delta Q^2} \times \frac{1}{\Delta x_B} \times \frac{1}{2\pi} \times n_{CM}(\boldsymbol{P}_{CM}) \times \frac{1}{4\pi},$$

and produces a list of events, each containing momentum vectors for a scattered electron ($\boldsymbol{p}_e$), a leading nucleon ($\boldsymbol{p}_N$), and a recoil nucleon ($\boldsymbol{p}_{recoil}$). The cross section for each event is calculated based on the integrand of Eq. 4 above and is given by:

$$\text{Eq. 7} \quad \frac{\mathrm{d}^8\sigma}{\mathrm{d}Q^2\, \mathrm{dx_B}\, \mathrm{d}\phi_{\mathrm{e}}\, \mathrm{d}^3\boldsymbol{P}_{CM}\, \mathrm{d}\Omega_{\mathrm{recoil}}} = \frac{\sigma_{eN}}{32\pi^4} \frac{\epsilon_N \epsilon_{recoil} \boldsymbol{p}_{recoil}^2\ \Theta(\boldsymbol{p}_{rel} - p_{rel}^{min}) n_{CM}(\boldsymbol{P}_{CM})}{|\epsilon_{recoil}(\boldsymbol{p}_{recoil} - \boldsymbol{Z} cos\theta_{z,recoil}) + \epsilon_N \boldsymbol{p}_{recoil}|} \frac{\omega}{2E_{beam}E_e x_B} \sum_\alpha C_\alpha |\tilde{\varphi}_{NN}^{\alpha}(\boldsymbol{p}_{rel})|^2 \quad ,$$

where $\boldsymbol{Z} \equiv \boldsymbol{q} + \boldsymbol{P}_{\mathrm{CM}}$ and $\theta_{Z,recoil}$ is the angle between $\boldsymbol{Z}$ and $\boldsymbol{p}_{recoil}$. For the case of pp pairs channels, C_α is equal to twice the nuclear contact for that channel. The starting weight w for each event is then given by $d\sigma/P$:

$$\text{Eq. 8} \qquad w = \frac{\sigma_{eN}}{4\pi^2} \Delta Q^2 \Delta x_B \frac{\epsilon_N \epsilon_{recoil} \boldsymbol{p}_{recoil}^2\ \Theta(\boldsymbol{p}_{rel} - p_{rel}^{min})}{|\epsilon_{recoil}(\boldsymbol{p}_{recoil} - \boldsymbol{Z} cos\theta_{z,recoil}) + \epsilon_N \boldsymbol{p}_{recoil}|} \frac{\omega}{2E_{beam}E_e x_B} \sum_\alpha C_\alpha |\tilde{\varphi}_{NN}^{\alpha}(\boldsymbol{p}_{rel})|^2.$$

The generation of events also includes electron radiation effects, introduced using the peaking approximation detailed in Ref. [41].

To compare our event generator to data, we take the following steps:

- Generate Monte Carlo events as explained above,
- Multiply the weight of each event by the CLAS detection efficiency for the particles detected in that event,
- Smear the generated electron and proton momenta to account for the CLAS resolution,

- Reject events with particles outside of the fiducial region of detected particles in CLAS,
- Apply the same event selection cuts used to select data-events.

We accounted for transparency and single-charge exchange (SCX) following Refs. [18, 20] by constructing the following relations:

$$\text{Eq. 9} \qquad \begin{aligned} \sigma^{Exp}_{A(e,e'pp)} = \; & \sigma^{GCF}_{A(e,e'pp)} \cdot P^{pp}_{A} \cdot T^{NN}_{A} + \\ & \sigma^{GCF}_{A(e,e'np)} \cdot P^{[n]p}_{A} \cdot T^{NN}_{A} + \\ & \sigma^{GCF}_{A(e,e'pn)} \cdot P^{p[n]}_{A} \cdot T^{NN}_{A}, \end{aligned}$$

$$\begin{aligned} \sigma^{Exp}_{A(e,e'p)} = \; & \left(\sigma^{GCF}_{A(e,e'pp)} + \sigma^{GCF}_{A(e,e'pn)}\right) \cdot P^{pp}_{A} \cdot T^{N}_{A} + \\ & \sigma^{GCF}_{A(e,e'np)} \cdot P^{[n]p}_{A} \cdot T^{N}_{A} + \\ & \sigma^{GCF}_{A(e,e'nn)} \cdot P^{[n]n}_{A} \cdot T^{N}_{A}, \end{aligned}$$

where σ^{GCF}_{X} are the GCF simulated events for process X without FSI or SCX, and the P_A and T_A factors are multiplied to the event weights to account for SCX and transparency probabilities, respectively. We note that the P_A and T_A factors do not impact the kinematics of the calculated events.

T^{NN}_{A} refers to the transparency for both the leading and recoil nucleons being emitted simultaneously, while T^{N}_{A} refers to the transparency for the leading nucleon independent of the recoil nucleon. We assume that the transparencies for protons and neutrons are the same, and therefore independent of SCX.

As SCX probabilities are different for protons and neutrons and high and low momentum, the *NN* superscript notation in the P factor mark the exact process being considered, such that particle with (without) square brackets are the ones that undergo (do not undergo) SCX. For example $P^{[p]p}_{A}$ is the probability that a leading proton in a pp pair undergoes SCX, $P^{p[p]}_{A}$ is this probability for the recoil proton and $P^{pp}_{A} = 1 - P^{[p]p}_{A} - P^{p[p]}_{A}$ is the probability that no proton undergoes SCX. As can be seen, SCX change final state neutrons to protons and vice versa. We note that we neglect cases where more than one particle undergoes SCX as these have negligible probability.

The values used for these probabilities are listed in Extended Data Table I.

Model Parameters and Systematic Uncertainties:

Uncertainty on the event-generator input parameters (e.g., CLAS resolution factors, transparency factors, SCX probabilities, Nuclear Contacts, SRC pair center-of-mass motion, A−2 system excitation energy, and the pair relative momentum value for the onset of the SRC regime) contributes to the systematic uncertainty of the calculation. We accounted for that by simulating a large number of "universes", in which these input parameters are each randomly drawn from prior probability distributions. We then examined the spread of the generator results across this space of universes to produce a systematic uncertainty band that captures 68% of the examined parameter combinations.

The following values and Gaussian uncertainties were used for these parameters (specific for ^{12}C):

- σ_{CM} , the gaussian width of the SRC pair center-of-mass momentum distribution [26]: 150 ± 20 MeV/*c*.
- The nuclear contacts for AV18, AV4' and N2LO(1fm) are taken from Ref. [25], specifically the k-space fits in the supplementary materials Table 1.
- SCX and nuclear transparency probabilities and uncertainties are given in Extended Data Table I, taken from Ref. [18] (SCX) and [14] (transparency).
- E^{*}_{A-2}, the excitation energy of the residual $A-2$ system, was varied uniformly between $0-30$ MeV.
- The p^{min}_{rel} cutoff in the universal two-body functions was varied uniformly between 250 and 350 MeV/*c*.
- The simulated electron resolution was varied uniformly between $1.0-1.5\%$.
- The simulated proton resolution was varied uniformly between $0.8-1.2\%$.
- The off-shell electron-nucleon cross section was chosen to be either σ_{CC1} or σ_{CC2} from Ref. [24].

Estimate of relativistic effects using the nuclear light-cone formalism:

The nuclear LC formalism allows accounting for relativistic effects in the two-body nuclear wave function. Its derivation is detailed in Ref. [9, 52, 53]. Here, we review its incorporation into the GCF model, the results of which are shown in the main text to assess the possible impact of relativistic effects.

In the LC formalism, standard momentum vectors are replaced by (α, $p_\perp$) where $p_\perp$ is the component of the momentum vector transverse to **q** and $\alpha \equiv \frac{\sqrt{m_N^2+p^2}-p_{||}}{m_A/A}$. Using these notations, the LC equivalent for the GCF universal functions are given by [9]:

$$\text{Eq. 10} \qquad \rho_{NN}^{\alpha}(\alpha_{rel}, p_{rel,\perp}) = \frac{|\tilde{\varphi}_{NN}^{\alpha}(k)|^2}{2-\alpha_{rel}} \sqrt{m_N^2 + k^2},$$

where

$$\text{Eq. 11} \qquad k^2 \equiv \frac{m_N^2+k_\perp^2}{\alpha_{rel}(2-\alpha_{rel})} - m_N^2$$

is the effective pair relative momentum probed relativistically, $k_\perp \equiv \frac{\alpha_i p_{recoil,\perp} - \alpha_{recoil} p_{i,\perp}}{\alpha_i + \alpha_{recoil}}$, and $\tilde{\varphi}_{NN}^{\alpha}$ are the non-relativistic universal functions defined previously, $p_{rel,\perp} \equiv \frac{1}{2}(p_{i,\perp} - p_{recoil,\perp})$, and $a_{rel} \equiv \frac{2\alpha_{recoil}}{\alpha_i + \alpha_{recoil}}$. Similarly, the SRC pair c.m. distribution is given by:

$$\text{Eq. 12} \qquad \rho_{CM}(\alpha_{CM}, p_{CM,\perp}) = \frac{(m_A/A)\alpha_{CM}}{(2\pi\sigma_{CM})^{3/2}} e^{-\frac{\left(\frac{m_A}{A}\right)^2 (2-\alpha_{CM})^2 + p_{CM,\perp}^2}{2\sigma_{CM}^2}},$$

Where $p_{CM,\perp} \equiv \boldsymbol{p}_{i,\perp} + \boldsymbol{p}_{recoil,\perp}$, and $\alpha_{cm} \equiv \alpha_i + \alpha_{recoil}$. Performing all appropriate variable substitutions and computing the relevant Jacobian, one finds that the LC equivalent of Eq. 7, i.e.:

$$\text{Eq. 13} \qquad \frac{d^8\sigma}{dQ^2\, dx_B\, d\phi_e\, d^3\boldsymbol{P}_{CM}\, d\Omega_{recoil}} =$$

$$\frac{\sigma_{eN}}{32\pi^4\alpha_i} \frac{\alpha_{A-2}}{\alpha_{CM}} \frac{\rho_{CM}(\alpha_{CM}, p_{CM,\perp})}{\epsilon_{A-2}} \frac{\epsilon_N \boldsymbol{p}_{recoil}^2\ \Theta\left(\boldsymbol{p}_{rel} - p_{rel}^{min}\right)}{\left|\epsilon_{recoil}(\boldsymbol{p}_{recoil} - \boldsymbol{Z}\cos\theta_{z,recoil}) + \epsilon_N \boldsymbol{p}_{recoil}\right|} \frac{\omega}{2E_{beam}E_e x_B} \frac{\sqrt{m_N^2+k^2}}{2-\alpha_{rel}} \sum_\alpha C_\alpha |\tilde{\varphi}_{NN}^{\alpha}(k)|^2,$$

which can be obtained by simply substituting into the right hand side of Eq. 7: $|\tilde{\varphi}_{NN}^{\alpha}(\boldsymbol{p}_{rel})|^2 \rightarrow \rho_{NN}^{\alpha}(\alpha, p_\perp)$ and $n_{CM}(\boldsymbol{P}_{CM}) \rightarrow \rho_{CM}(\alpha_{CM}, p_{CM,\perp})$ and by inserting the necessary Jacobian factors resulting from the transformation from **p** to (α,$p_\perp$). Following these modifications, the rest of the LC calculation follows exactly the non-relativistic description above.

The importance of relativistic effects at high-momenta can be seen by considering the simple case of scattering off a forward vs. backward going nucleon in the deuteron. Without accounting for relativistic effects, in the forward scattering case (i.e. recoil nucleon at 180° to **q**) the maximally allowed momenta of the recoil nucleon equals $(3/4)m_N$, while in the backward scattering case (i.e. recoil nucleon at 0° to **q**) there is no kinematical restriction on the momenta of the recoil nucleon. The LC formalism presented above removes this asymmetry [9].

As mentioned in the main text, while studied in detail [9, 52, 53] and used by previous works to analyze proton induced knockout reactions [17], the LC prescription used here to account for relativistic effects is approximate and model-dependent. The accuracy of Eq. 10 was previously studied by Ref. [51] using simple covariant models for which the four-dimensional solution of the Bethe-Salpeter wave function can be obtained, to find that for these models Eq. 10 requires corrections on the scale of 5% - 10% for the kinematics of the current experiment. This is encouraging; however, these estimations are based on simple models and should be extended in the future for more realistic interactions.

Measurement Kinematics and Reaction Mechanism Effects:

Experimentally, we measure final-state particles and reconstruct the initial state of the nucleons, before the electron interaction, based on modeling of the electron scattering reaction. This work focuses on the specific interpretation of the data in terms of QE electron scattering from a single nucleon, as shown in Extended Data Fig. 2. However, as shown by previous studies, the reaction can also include contributions from (1) meson-exchange currents (MEC), (2) isobar currents (exciting the struck nucleon to an intermediate excited state), (3) elastic and inelastic nucleon rescattering (final-state interactions, FSIs), and (4) single charge exchange (SCX) reactions, that would all lead to a similar final state as the QE scattering reaction. The relative contribution of these reaction mechanisms depends on the kinematics of the experiment [19 – 21, 42 - 46], see Ref. [8] and references therein for a detailed discussion and review of previous experimental and theoretical studies.

MEC are suppressed as $1/Q^2$ compared to SRC pair breakup, and their contribution in our kinematics is therefore small. Isobar currents are suppressed for $x_B > 1$, as, for a given Q^2, the virtual photon transfers less energy and is less likely to excite the nucleon to an isobar current.

For high missing momentum events, elastic FSIs include rescattering of the outgoing nucleon with the other nucleon of the SRC pair or with the other nucleons in the residual nucleus. At large knock-out nucleon momenta, such rescattering, as well as SCX interactions, can be estimated using a generalized Eikonal approximation in a Glauber framework [20, 21, 47], previously shown to well-reproduce experimental data [27 - 29]. These calculations show that in our kinematics, elastic FSIs are largely confined to nucleons in close proximity, and the largest part of the scattering cross section can be attributed to rescattering between nucleons of the SRC pair [48]. Therefore, FSI predominantly leads to flux reduction that can be quantified in terms of a transparency factor.

SCX can turn proton knockout events into neutron knockout events via (*p,n*) processes, which reduces the yield and is accounted for as part of the transparency factors. SCX can also turn neutron knockout events into (*e,e'p*) events via (*n,p*) reactions, which increases the yield.

In addition, rescattering between the knockout and recoil nucleons (i.e. the nucleons of the pair) can also distort the kinematics of the measured events. Previous studies of the deuteron shows that in the kinematics of the current measurement, such internal pair rescattering is strongly suppressed [46].

Thus, the two main reaction mechanisms that effect our measurement are transparency reductions and SCX enhancements due to neutron knockout interactions.

One should note that this simple QE picture, with suppressed elastic FSIs, is strongly supported by the fact that it describes well both high-Q^2 electron-scattering data and high-energy proton scattering data [17, 40], that have very different reaction mechanisms. In addition, the results of the electron and proton-scattering experiments give consistent SRC-pair isospin ratios [14, 17, 18] and CM momentum distributions [26, 39, 40].

Tests of Contributions from Non-QE Reaction Mechanisms:

Non-QE reaction mechanisms, beyond those accounted for by the SCX and transparency corrections, such as small-angle leading-nucleon rescattering, can modify the measured kinematics and therefore interfere with the interpretation of the data. By changing the leading-nucleon momentum, rescattering can cause events with high missing-momentum that originate from interactions with low initial-momentum nucleons. We performed several experimental tests of these effects.

(1) Rescattering should increase with atomic mass, but the properties of SRCs should be very similar for different nuclei [7 – 9, 48]. Therefore we examined the nuclear mass (A) dependence of the data, for A = 12 (C), 27 (Al), 56 (Fe), and 208 (Pb). See Extended Data Figs. 3-5 for the missing momentum, x_B, Q^2 and angle between missing-momentum and momentum transfer (q) of the measured A(*e,e'p*) and A(*e,e'pp*) event yields, as well as for the missing momentum dependence of the measured A(*e,e'pp*) / A(*e,e'p*) yield ratio. In all cases the data for the different nuclei are very similar, indicating that A-dependent effects are small.

(2) Leading-nucleon rescattering would give a peak in the $\theta_{p_{miss}q}$ (the angle between the momentum transfer and the missing momentum) distribution at 110° (non-relativistically, that peak would be at 90°) [8, 21]. Extended Data Fig. 4 shows the $\theta_{p_{miss}q}$ distribution for all four nuclei and the GCF ^{12}C calculations. There is no peak in either the data or the calculation at the expected rescattering maximum. In addition, the $\theta_{p_{miss}q}$ distributions are similar for all nuclei, whereas rescattering should increase with A. These are further indications that rescattering is small for this data.

(3) Light-cone momentum densities are sensitive to longitudinal momentum components relative to the momentum transfer [19, 21]. Calculations show that while nucleons that undergo rescattering change both their energy and momenta, at large-Q^2 and anti-parallel kinematics the difference between the nucleon energy and its momentum component along the q vector direction, which is proportional to its light-cone momentum, is approximately conserved [21]. Therefore, we expect for light-cone momentum distributions to be well reproduced by the GCF calculation.

The light-cone momentum fraction carried by the interacting nucleon is defined as: $\alpha_{miss} \equiv \alpha_N - \alpha_q$, where $\alpha_N \equiv \frac{E_N - p_N^{\hat{q}}}{m_A/A}$ and $\alpha_q \equiv \frac{\omega - q}{m_A/A}$. Extended Data Fig. 10 shows the distribution of α_{miss} for (*e,e'p*) and (*e,e'pp*) reactions for both data and GCF calculations. For completeness, it also shows the light-cone pair CM momentum distribution $\alpha_{c.m.} \equiv \alpha_N + \alpha_{recoil}$ (where $\alpha_{recoil} \equiv \frac{E_{recoil} - p_{recoil}^{\hat{q}}}{m_A/A}$) for the (*e,e'pp*) reaction for both data and GCF calculations. α_{miss} ranges from 1.2 to about 1.6, spanning the expected range for 2N-SRC pairs dominance [19]. $\alpha_{c.m.}$ is centered around the expected value of 2. As expected, all light-cone momentum distributions show overall good agreement between the data and calculations.

(4) As the data and calculations shown in Extended Data Fig. 4 are integrated over missing momentum, they are dominated by low missing-momentum, potentially masking issues at high missing momentum. To address this, Extended Data Figs. 8 and 9 show the distribution of the components of the missing momentum in the direction longitudinal and transverse to the momentum-transfer q, in bins of missing momentum for the (*e,e'p*) (Fig. 8) and *(e,e'pp)* (Fig. 9) reactions for both data and GCF calculations. In all missing-momentum bins, the data and

simulation show good agreement, and the kinematics are predominantly anti-parallel with the longitudinal component being larger than the transverse.

To supplement the light-cone momentum density discussed in point (3) above (which is sensitive to the longitudinal component of the missing momentum), we also note that we do not see any enhancement of the transverse component of the missing momentum, as compared with the GCF expectation. Such enhancement is a typical signature of small-angle elastic scattering, which is not included in the GCF calculation but could be present in the data. The agreement of the data with the GCF calculation suggest that such scattering does not contribute significantly to the data.

(5) Lastly, we note the different missing momentum dependence of the measured and simulated *(e,e'p)* and *(e,e'pp)* event yields. As can be seen in Fig. 2, while the *(e,e'p)* distribution falls over two orders of magnitude, the *(e,e'pp)* distribution is much flatter and only varies over one order of magnitude. If both distributions were driven by rescattering of low initial-momentum nucleons as they exit the nucleus, leading to the emission of a recoil nucleon and formation of large missing momentum, both distributions should have similar missing-momentum distributions.

We note that all conclusions mentioned above hold true also when relativistic corrections are introduced to the calculations.

Initial Nucleon Energy:

We use the convention that the spectral function depends on ϵ_i, the initial off-shell energy of the struck nucleon prior to scattering. The expected initial off-shell energy for nucleons in a stationary pair is given by: $\epsilon_i = m_A - m_{A-2} - \sqrt{p_i^2 + m_N^2}$, which is shown by purple arrows in Fig. 3.

Scalar Limit Estimation:

The general expectation for a fully scalar *NN* interaction and a symmetric nucleus, is that the abundance of pairs will be equal for all isospin, spin, and spin-projection states. This implies that the number of spin-1 pn-SRC pairs should be three times the number of spin-0 pp-, pn-, and nn-pairs due to the three possible spin orientations. Therefore, simple counting implies:

$$\text{Eq. 14} \qquad \frac{\#e'pp}{\#e'p} = \frac{2N_{pp}^{s=0}}{2N_{pp}^{s=0}+N_{pn}^{s=0}+N_{pn}^{s=1}} = \frac{2N^{s=0}}{(2+1+3)N^{s=0}} = \frac{1}{3},$$

where $N_{NN}^{s=S}$ is the number of *NN* pairs in a spin S state. This limit is shown as the dashed line labeled 'scalar limit' in Extended Data Fig. 12 (a).

Cutoff Dependence and Non-Local Chiral Interactions:

In addition to the local interactions studied in this work, nuclear structure calculations are often performed using non-local interactions, that feature different high-momentum asymptotic behavior as compared to the local ones. The Chiral-EFT versions of these interactions have momentum-space cutoffs and are considered to be 'softer' than the local interactions studied here.

The main limitation for studying such interactions using the GCF framework presented here is that, at the moment, there are no available calculations of the two-nucleon momentum distribution in ^{12}C using these interactions. Therefore, we are unable to determine the nuclear contacts for these interactions in a fully theoretical fashion as is done for the local interactions considered above.

One previous work [12] studied the non-local N3LO(600 MeV/*c*) interaction [5] using the GCF by extracting the ratio of spin-1 to spin-0 contacts from a fit to the experimental data of Refs. [14, 15]. While this procedure can't be compared on equal footing with the fully theoretical predictions we have for the local-interactions, it is still interesting to see how they compare with each other and with the data. This comparison is shown in Extended Data Fig. 11, which is equivalemt to Fig. 2 of the main text. As can be seen, the non-local N3LO(600 MeV/*c*) interaction seems to reproduce the experimental data well up to its cutoff, but then decays faster than the local interactions. This is an encouraging observation as the 600 MeV/*c* cutoff of this interaction is well above the 350 MeV/*c* cutoff of the *NN* phase-shifts used in its construction.

It is interesting to note that its predictions are quite similar to those of the N2LO(1.2 fm) interaction. Future studies will focus on using the experimental data provided in this work (which is much more detailed than that of Refs. [14, 15]) to fit the nuclear contacts for different local and non-local interactions and study the dependence of the results on the chiral expansion order and cutoff.

For completeness, we note that from a theoretical standpoint, the reaction diagram used for the GCF calculations and shown in Extended Data Fig. 2 can be viewed as a 'high-resolution' starting point for a unitary-transformed calculation [50]. As a thought exercise, the χEFT NN interactions used here can be considered as resulting from applying unitary transformations to models that have shorter distance / higher-momentum cutoffs. As this process would introduce many-body interaction currents to the description of the electron scattering reaction, the use of a high-resolution (one-body) reaction description with χEFT interactions, as done in this work, is non-trivial. This is one explanation for the disagreement between the data and calculations at high p_{miss}. The data presented here can therefore quantify the importance of such many-body effects and demonstrate that they become significant only above the cutoff for non-relativistic calculations and at much higher momenta when relativistic effects are accounted for. This can help guide future studies of effects such as relativity and non-nucleonic degrees of freedom.

Additional References:

[31] "A Double Target System for Precision Measurements of Nuclear Medium Effects", H. Hakobyan et al., Nucl. Inst. and Meth. A **592**, 218 (2008).

[32] "Short range correlations and the isospin dependence of nuclear correlation functions", R. Cruz-Torres, A. Schmidt, G.A. Miller, L.B. Weinstein, N. Barnea, R. Weiss, E. Piasetzky, and O. Hen, Phys. Lett. B 785, 304 (2018).

[33] "Short-range correlations and the charge density", R. Weiss, A. Schmidt. G.A. Miller, and N. Barnea, Phys. Lett. B **790**, 484 (2019).

[34] "Exclusive electrodisintegration of ^{3}He at high Q^2 II. Decay function formalism" M.M. Sargsian, T. V. Abrahamyan, M. I. Strikman, and L. L. Frankfurt, Phys. Rev. C 71, 044615 (2005).

[35] "Single- and two-nucleon momentum distributions for local chiral interactions", D. Lonardoni, S. Gandolfi, X. B. Wang, and J. Carlson, Phys. Rev. C **98**, 014322 (2018).

[36] "Nucleon and nucleon-pair momentum distributions in A ≤ 12 nuclei", R.B. Wiringa, R. Schiavilla, S.C. Pieper, and J. Carlson, Phys. Rev. C **89**, 024305 (2014).

[37] "Realistic model of the nucleon spectral function in few and many nucleon systems", C. Ciofi degli Atti and S. Simula, Phys. Rev. C **53**, 1689 (1996).

[38] "Factorization of exclusive electron-induced two-nucleon knockout", C. Colle, W. Cosyn, J. Ryckebusch, and M. Vanhalst, Phys. Rev. C **89**, 024603 (2014).

[39] "Investigation of proton-proton short-range correlations via the ^{12}C(*e,e'pp*) reaction", R. Shneor et al. (Jefferson Lab Hall A Collaboration), Phys. Rev. Lett. **99**, 072501 (2007).

[40] "n-p short range correlations from (p,2p + n) measurements", A. Tang et al (EVA Collaboration), Phys. Rev. Lett. **90**, 042301 (2003).

[41] "Radiative corrections for (*e,e'p*) reactions at GeV energies", R. Ent, B.W. Filippone, N.C.R. Makins, R.G. Milner, T.G. O'Neill, and D.A. Wasson, Phys. Rev. C **64**, 054610 (2001).

[42] "Feynman graphs and generalized eikonal approach to high energy knock-out processes", L.L. Frankfurt, M.M. Sargsian, and M.I. Strikman, Phys. Rev. C **56**, 1124 (1997).

[43] "Quasielastic ^{3}He(*e,e'p*)^{2}H Reaction at Q^2 = 1.5 GeV^2 for Recoil Momenta up to 1 GeV/*c*", M. Rvachev et al. Phys. Rev. Lett. **94**, 192302 (2005).

[44] "Measurement of the ^{3}He(*e,e'p*)pn Reaction at High Missing Energies and Momenta", F. Benmokthar et al. Phys. Rev. Lett. **94**, 082305 (2005).

[45] "Experimental Study of Exclusive ^{2}H(*e,e'p*)n Reaction Mechanisms", K. S. Egiyan et al. (CLAS Collaboration), Phys. Rev. Lett. **98**, 262502 (2007).

[46] "Probing the High Momentum Component of the Deuteron at High Q^2", W.U. Boeglin et al. Phys. Rev. Lett. **107**, 262501 (2011).

[47] "Color transparency: past, present and future", D. Dutta, K. Hafidi, and M. Strikman, Prog. Part. Nucl. Phys. **69**, 1 (2013).

[48] "Universality of many-body two-nucleon momentum distributions: Correlated nucleon spectral function of complex nuclei", C. Ciofi degli Atti and H. Morita, Phys. Rev. C **96**, 064317 (2017).

[49] R. Cruz-Torres, D. Lonardoni, private communication.

[50] "Scale dependence of deuteron electrodisintegration", S. N. More, S. K. Bogner, and R. J. Furnstahl, Phys. Rev. C **96**, 054004 (2017).

[51] "Relation between equal-time and light-front wave functions", G.A. Miller and B.C. Tiburzi, Phys. Rev. C **81**, 035201 (2010).

[52] "Short range correlations in nuclei as seen in hard nuclear reactions and light cone dynamics", L. Frankfurt and M. Strikman, Modern topics in electron scattering, B. Frois (ed.), I. Sick (ed.), 645-694, (1992).

[53] “Multinucleon short-range correlation model for nuclear spectral functions: Theoretical framework”, O. Artiles and M. Sargsian, Phys. Rev. C **94**, 064318 (2016).

Acknowledgements We acknowledge the efforts of the staff of the Accelerator and Physics Divisions at Jefferson Lab that made this experiment possible. The analysis presented here was carried out as part of the Jefferson Lab Hall B Data-Mining project supported by the U.S. Department of Energy (DOE). The research was supported also by the National Science Foundation, the Israel Science Foundation, the Pazi foundation, the Chilean Comisión Nacional de Investigación Científica y Tecnológica, the French Centre National de la Recherche Scientifique and Commissariat a l’Energie Atomique, the French-American Cultural Exchange, the Italian Istituto Nazionale di Fisica Nucleare, the National Research Foundation of Korea, and the UKs Science and Technology Facilities Council. Jefferson Science Associates operates the Thomas Jefferson National Accelerator Facility for the DOE, Office of Science, Office of Nuclear Physics under contract DE-AC05-06OR23177.

Author Contributions The CEBAF Large Acceptance Spectrometer was designed and constructed by the CLAS Collaboration and Jefferson Lab. Data acquisition, processing and calibration, Monte Carlo simulations of the detector, and data analyses were performed by a large number of CLAS Collaboration members, who also discussed and approved the scientific results. The analysis presented here was performed primarily by A.S and J.P. R.W. and N.B. provided theoretical input and helped implement parts of the GCF event generator. M.S. and A.L. provided theoretical input and helped implement the Light Cone Formalism. A.D. and E.S. helped implement parts of the GCF event generator and performed the model systematic uncertainty studies. A.H. calculated the CLAS acceptance maps. O.H., E.P., and L.B.W. guided and supervised the analysis.

Author Information Reprints and permissions information is available at www.nature.com/reprints. The authors declare no competing financial interests. Readers are welcome to comment on the online version of the paper. Publisher’s note: Springer Nature remains neutral with regard to jurisdictional claims in published maps and institutional affiliations. Correspondence and requests for materials should be addressed to O.H. (hen@mit.edu).

Author List

A. Schmidt,[1] J. Pybus,[1] R. Weiss,[2] E.P. Segarra,[1] A. Hrnjic,[1] A. Denniston,[1] O. Hen,[1,+] E. Piasetzky,[3] L.B. Weinstein,[4] N. Barnea[2] M. Strikman[5], A. Larionov[6], D. Higinbotham[7] and the CLAS Collaboration.

[1]Massachusetts Institute of Technology, Cambridge, MA 02139, USA
[2]Hebrew University, Jerusalem, Israel
[3]Tel Aviv University, Tel Aviv, Israel
[4]Old Dominion University, Norfolk, Virginia 23529, USA
[5]Pennsylvania State University, University Park, PA 16802, USA
[6]Frankfurt Institute for Advanced Studies, Giersch Science Center, D-60438 Frankfurt am Main, Germany
[7]Thomas Jefferson National Accelerator Facility, Newport News, Virginia 23606, USA
[+]Contact Author: hen@mit.edu

Extended data:

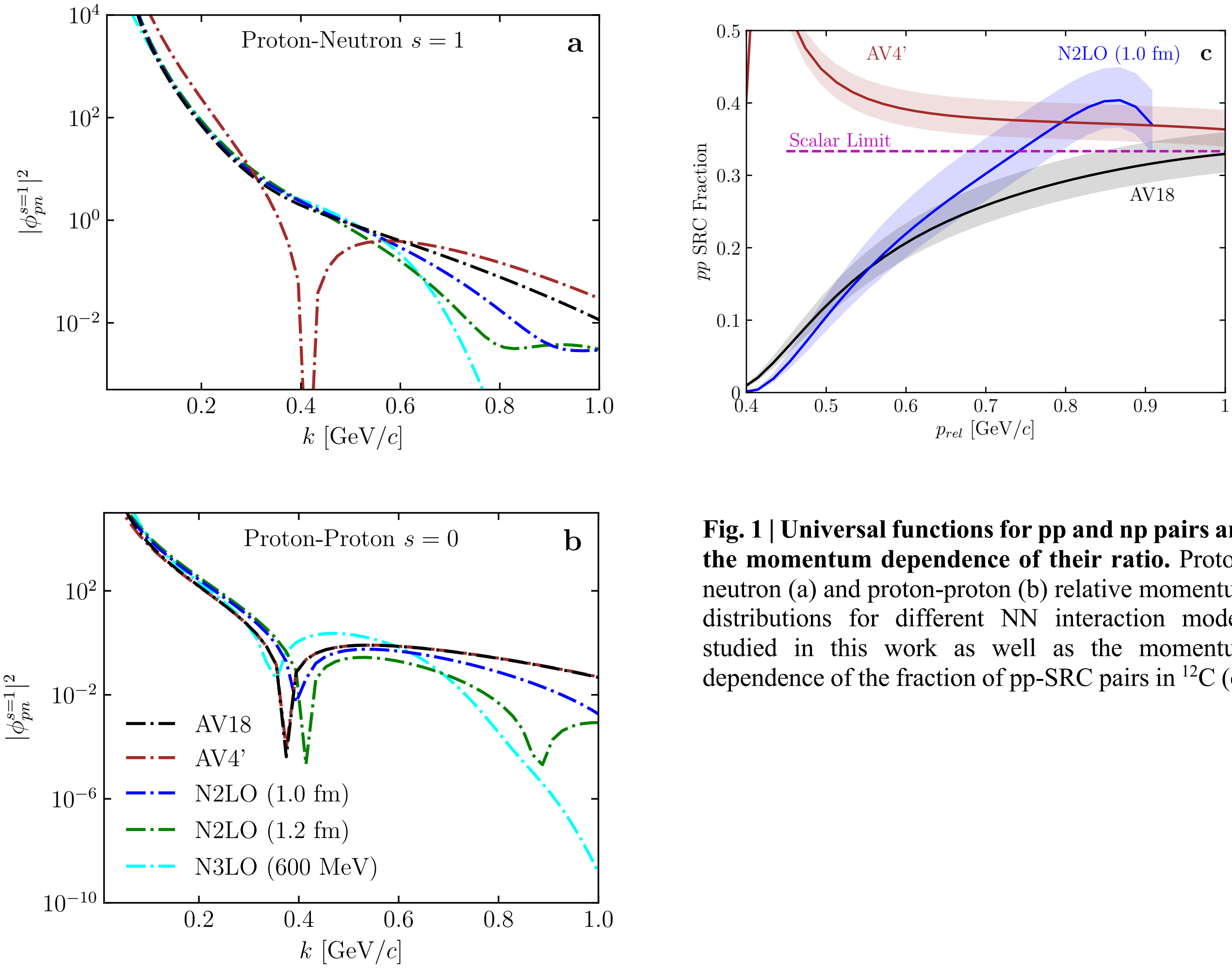

Fig. 1 | Universal functions for pp and np pairs and the momentum dependence of their ratio. Proton-neutron (a) and proton-proton (b) relative momentum distributions for different NN interaction models studied in this work as well as the momentum dependence of the fraction of pp-SRC pairs in ^{12}C (c).

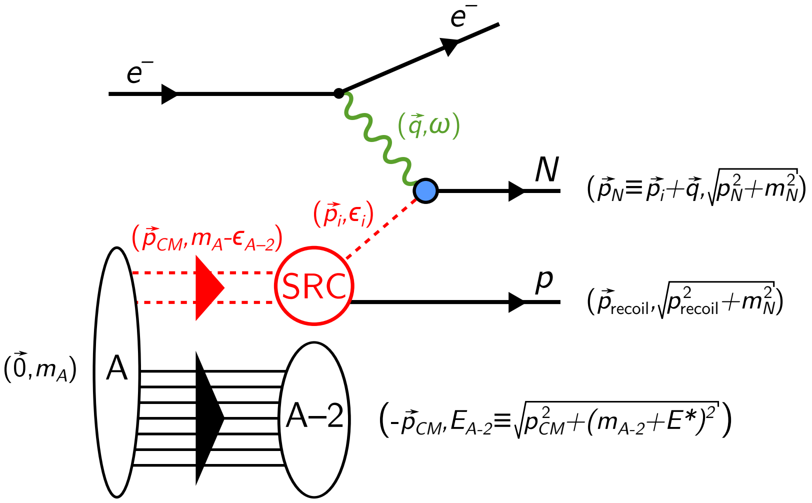

Fig. 2 | SRC pair breakup: Diagrammatic representation and 4-momentum kinematics of two-nucleon knockout $A(e,e'Np)$ reaction, within the SRC model. Dashed red lines represent off-shell particles and solid black lines mark detected particles. The A-2 system is undetected.

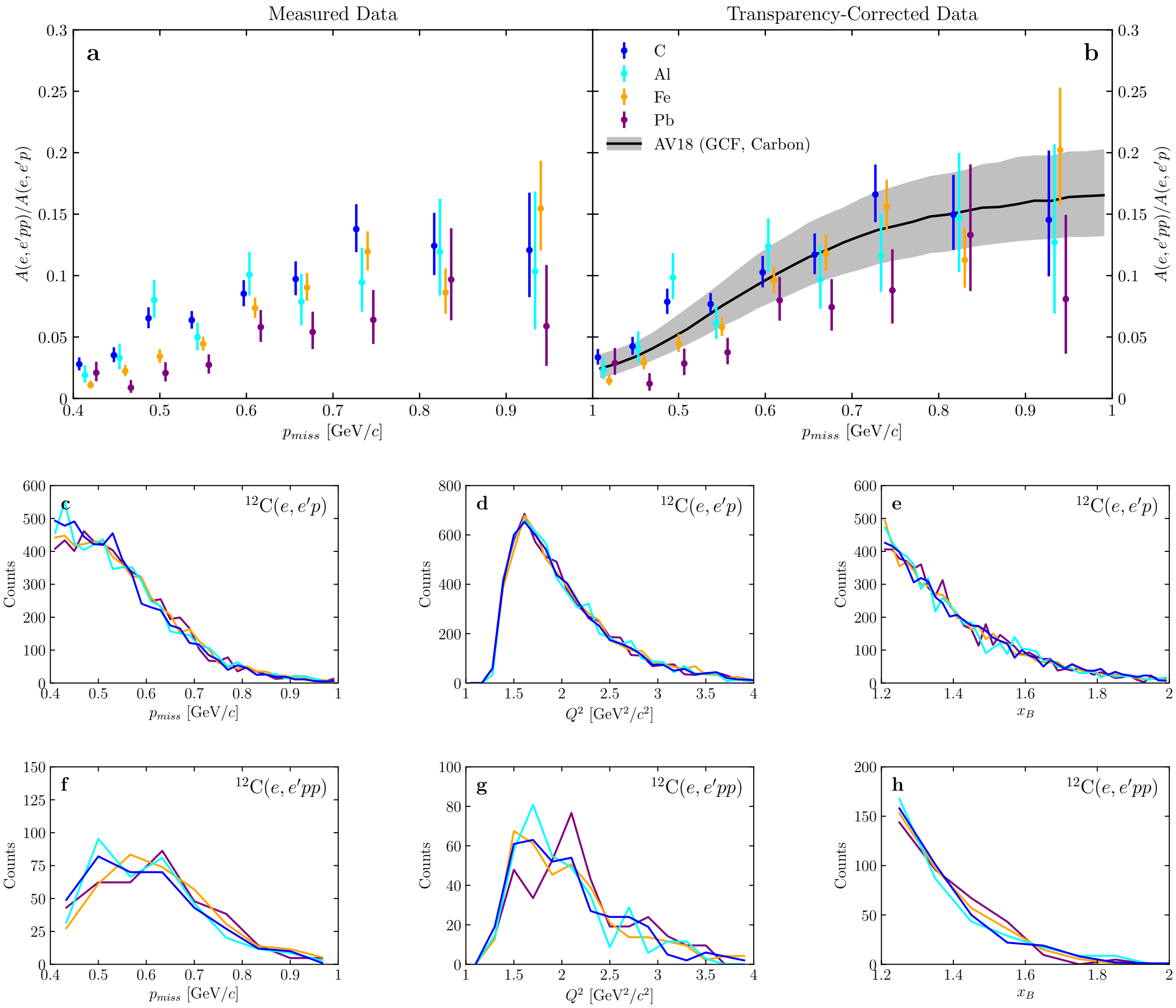

Fig. 3 | Kinematical distributions and A(*e,e'pp*) / A(*e,e'p*) ratios for A = 12 – 208 Nuclei: Measured ratio of A(*e,e'pp*) / A(*e,e'p*) relative event yield as a function of reconstructed (*e,e'p*) missing momentum for A = 12 (C), 27 (Al), 56 (Fe) and 208 (Pb), before (a) and after (b) transparency corrections. The band shows the result of the theoretical GCF calculation for ^{12}C using the AV18 interaction. The width of the band and the data error bars show the model systematic uncertainties and data statistical uncertainties, respectively, each at the 1σ or 68% confidence level. c - h: Comparison of the kinematical distribution of (*e,e'p*) missing momentum (c, f), Q^2 (d, g) and x_B (e, h) for A(*e,e'p*) (c-e) and A(*e,e'pp*) (f-h) reactions. The total number of counts in Al, Fe, and Pb was scaled to match that of C.

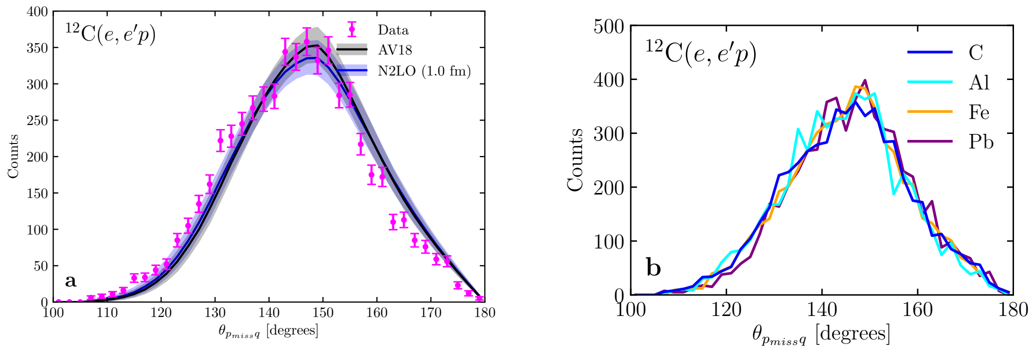

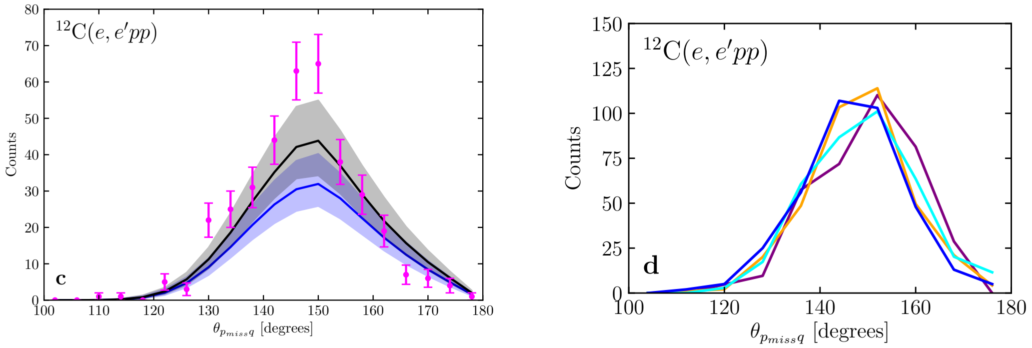

Fig. 4 | Momentum-transfer and missing-momentum angular correlations: Distribution of the relative angle between the momentum transfer q and (*e,e'p*) missing momentum for A(*e,e'p*) (top) and A(*e,e'pp*) (bottom) reactions. Left: Comparison of ^{12}C data and GCF calculations using different *NN* interaction models (colored bands). Right: Comparison of data for A = 12 (C), 27 (Al), 56 (Fe), and 208 (Pb) nuclei. The width of the band and the data error bars show the model systematic uncertainties and data statistical uncertainties, respectively, each at the 1σ or 68% confidence level.

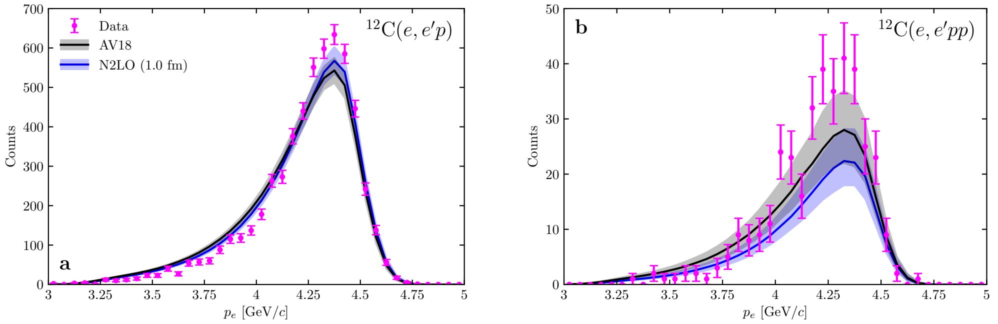

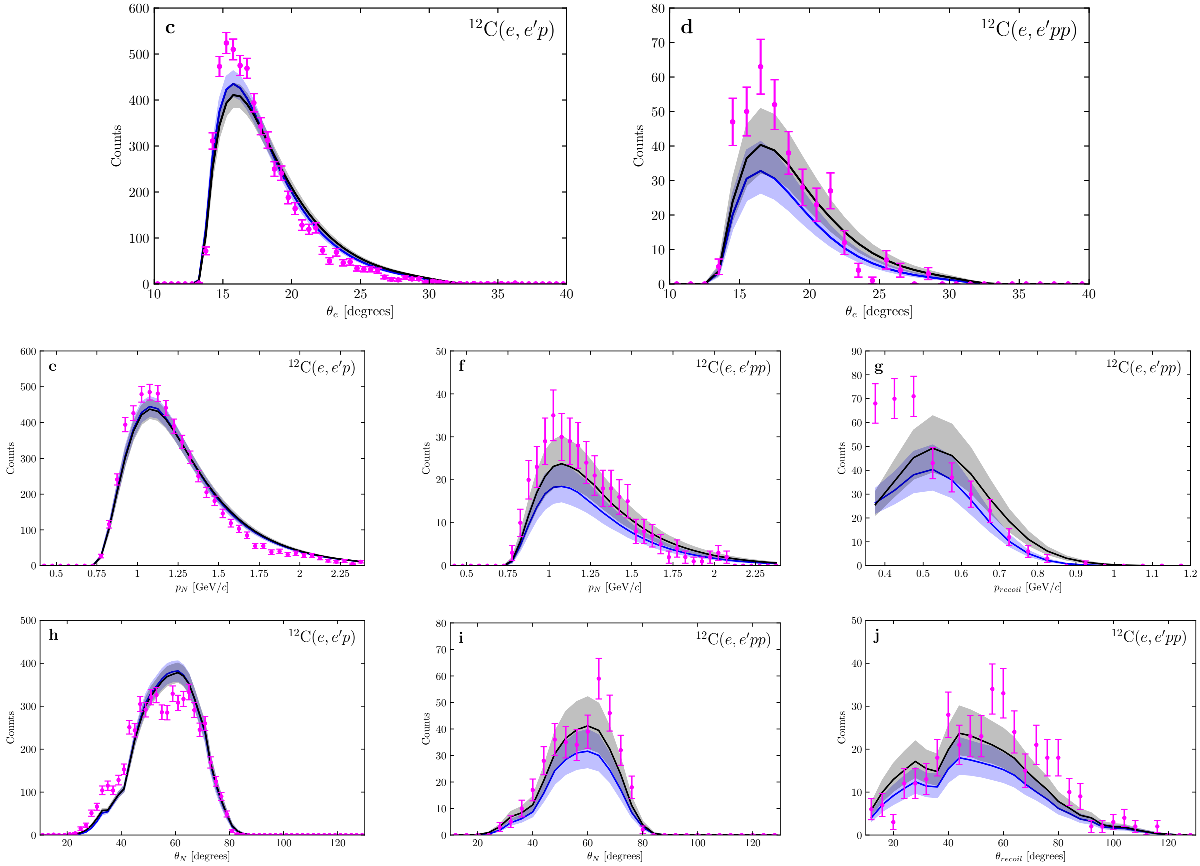

Fig. 5 | Electron and proton kinematics: Scattered electron and proton momentum and angle distributions for ^{12}C(*e,e'p*) (a, c, e, h) and ^{12}C(*e,e'pp*) (b, d, f, g, i, j) events. Colored bands show GCF calculations. The width of the band and the data error bars show the model systematic uncertainties and data statistical uncertainties, respectively, each at the 1σ or 68% confidence level.

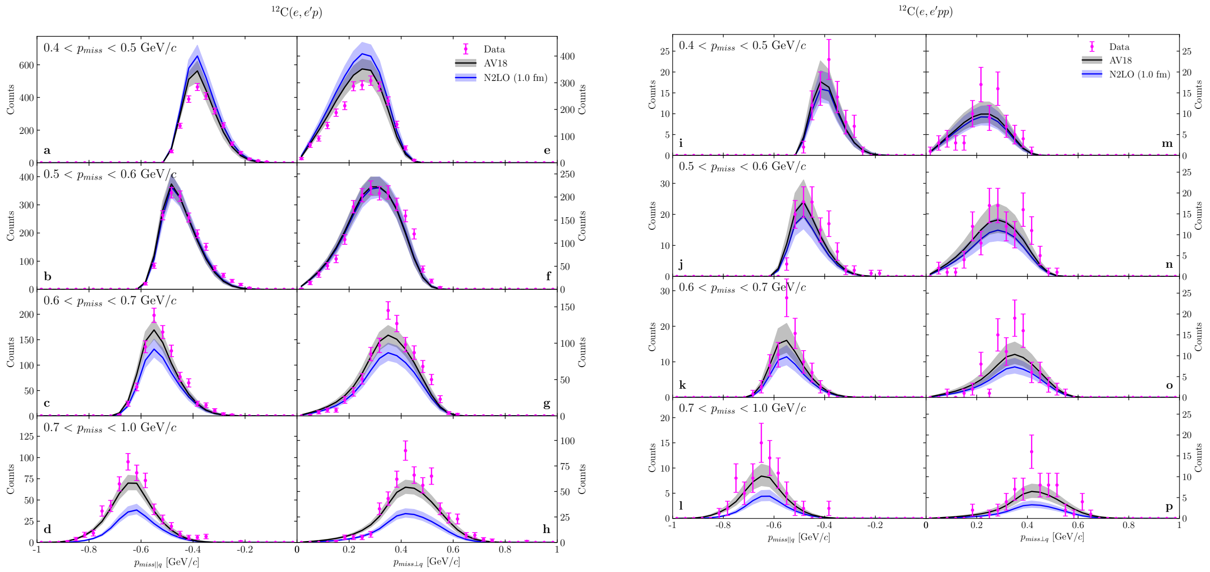

Fig. 6 | Missing momentum components for ^{12}C(*e,e'p*) and ^{12}C(*e,e'pp*) events: Distributions of the components of the ^{12}C(*e,e'p*) (a - h) and ^{12}C(*e,e'pp*) (i - p) missing momentum parallel (a – d, i - l) and perpendicular (e - h, m - p) to the momentum transfer q for different missing-momentum vector magnitudes. Colored bands show GCF calculations using different *NN* interaction models The width of the band and the data error bars show the model systematic uncertainties and data statistical uncertainties, respectively, each at the 1σ or 68% confidence level.

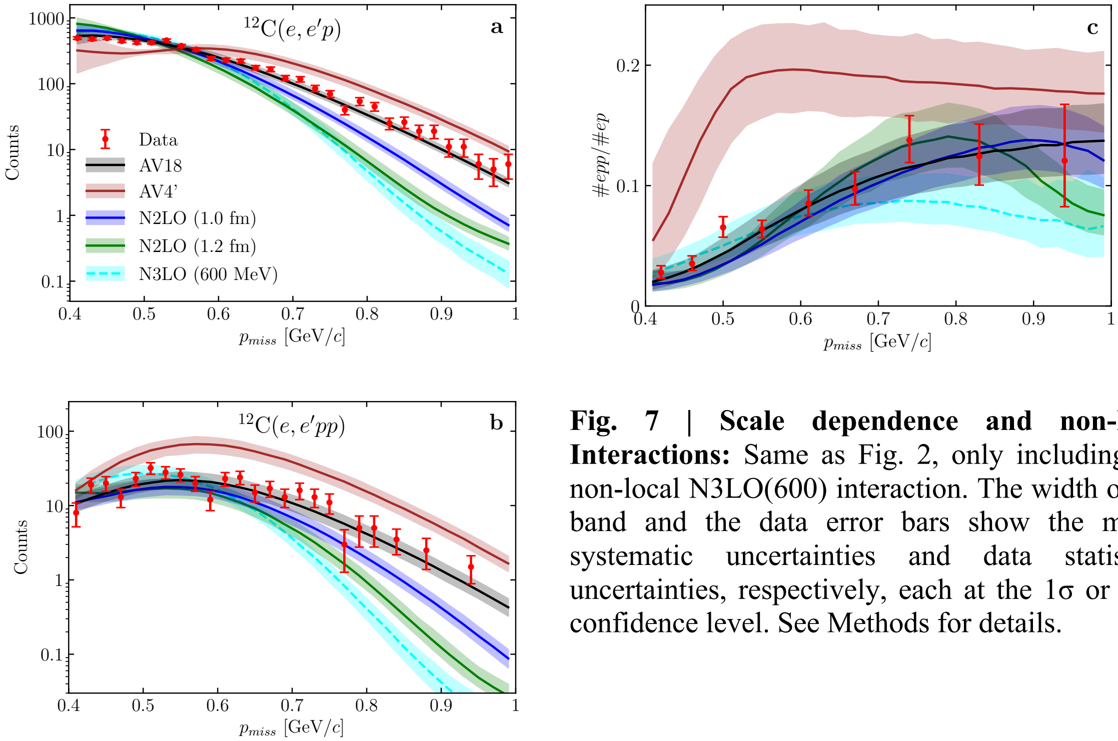

Fig. 7 | Scale dependence and non-local Interactions: Same as Fig. 2, only including the non-local N3LO(600) interaction. The width of the band and the data error bars show the model systematic uncertainties and data statistical uncertainties, respectively, each at the 1σ or 68% confidence level. See Methods for details.

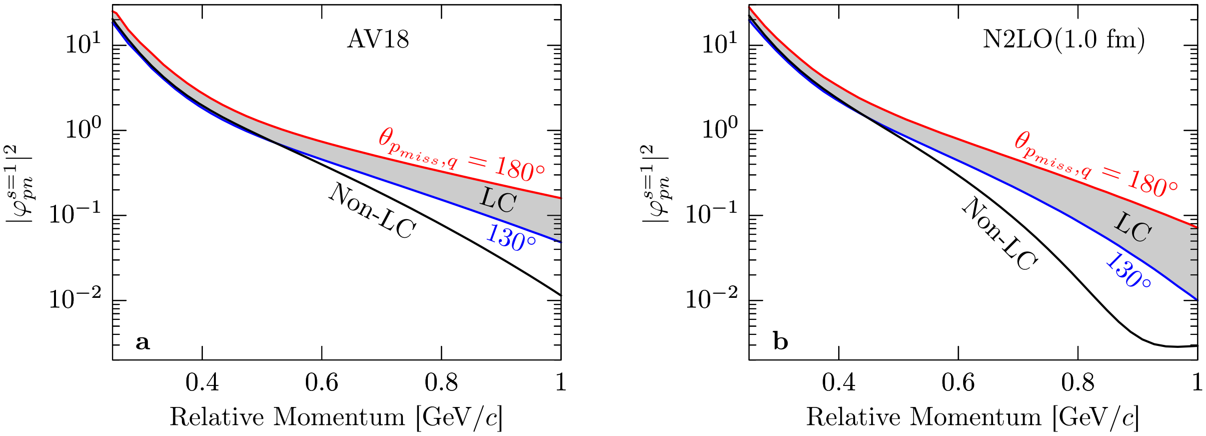

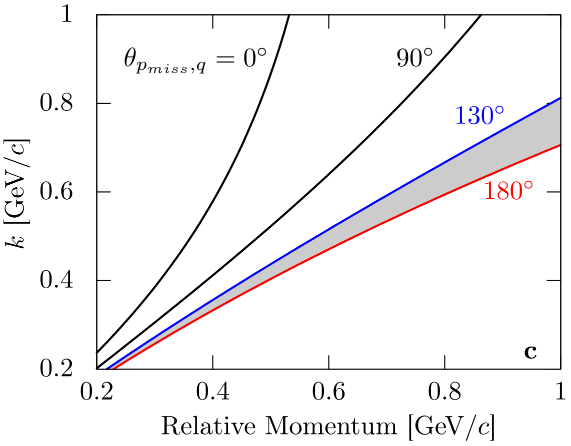

Fig. 8 | Relative Momenta in Light-Cone Formalism. Bottom Left: the LC relative momentum variable, k, vs. the non-relativistic relative momentum for several different angles between $\boldsymbol{p_{miss}}$ and $\boldsymbol{q}$. The kinematics from this measurement are shown by the gray band. Top: the effective relative momentum distribution calculated for the AV18 (a) and N2LO(1.0) (b) potentials in non-LC (black line) and LC (gray band) approaches for the range of $\theta_{p_{miss},q}$ angles as in the data. The LC distribution is larger in the high-momentum tail region because k is smaller than the relative momentum.

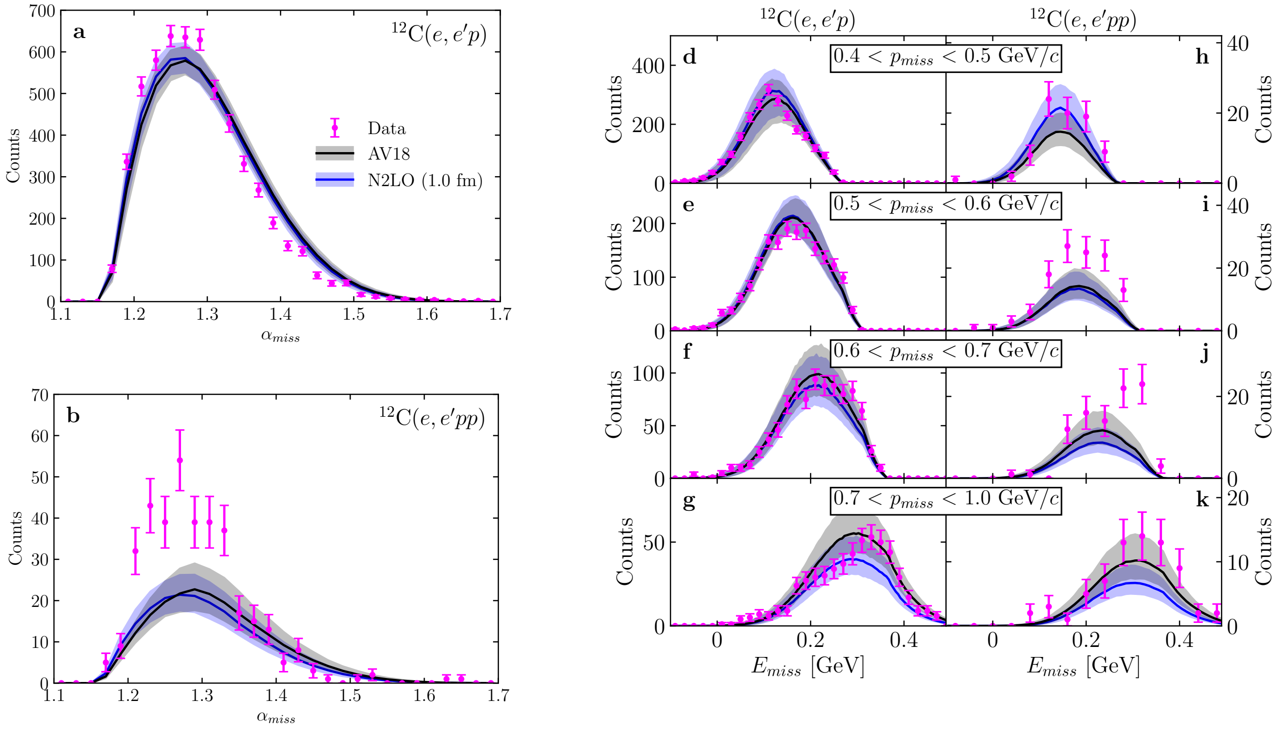

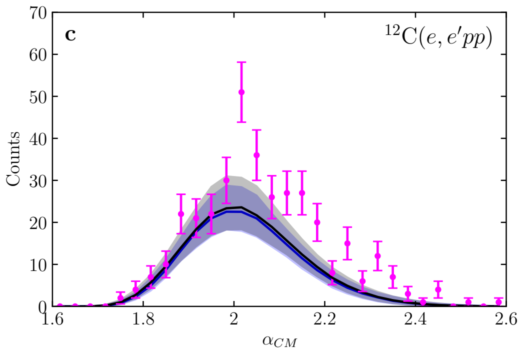

Fig. 9 | LC Calculations of the nuclear spectral function and LC momentum fractions. The reconstructed initial light-cone momentum fraction carried by the struck nucleon for (*e,e'pp*) (a) and (*e,e'p*) (b) events as well as the total pair light-cone momentum fraction for (*e,e'pp*) events (c) and the spectral function (d-k). Bands show GCF calculations using LC formalism. The width of the band and the data error bars show the model systematic uncertainties and data statistical uncertainties, respectively, each at the 1σ or 68% confidence level.

Table 1 | Single Charge Exchange and Transparency Probabilities: calculated for ^{12}C.

P^{pp}	$P^{[p]p}$	$P^{p[p]}$	$P^{[pp]}$	$P^{p[n]}$	$P^{[p]n}$	P^{np}	$P^{[n]p}$	$P^{n[p]}$	$P^{[np]}$	$P^{n[n]}$	T^{N}	T^{NN}
90.8% ± 0.6%	4.1% ± 0.3%	4.8% ± 0.3%	0.3% ± 0.02%	4.1% ± 0.3%	3.5% ± 0.2%	92.2% ± 0.5%	3.5% ± 0.2%	4.1% ± 0.3%	0.2% ± 0.01%	4.8% ± 0.3%	53% ± 5%	44% ± 4%

University of Virginia, Charlottesville, VA 22901

DRAFT: Author List

A. Schmidt,[1] J. Pybus,[1] R. Weiss,[2] E.P. Segarra,[1] A. Hrnjic,[1] A. Denniston,[1] O. Hen,[1] E. Piasetzky,[3] L.B. Weinstein,[4] N. Barnea,[2] S. Adhikari,[15] Giovanni Angelini,[17] H. Atac,[39] H. Avakian,[40] C. Ayerbe Gayoso,[48] L. Baashen,[15] L. Barion,[19] M. Bashkanov,[45] M. Battaglieri,[21] I. Bedlinskiy,[30] F. Benmokhtar,[50] A. Bianconi,[43,24] A.S. Biselli,[13,8] F. Bossù,[10] S. Boiarinov,[40] M. Brahim,[51] W.J. Briscoe,[17] V.D. Burkert,[40] F. Cao,[11] D.S. Carman,[40] J.C. Carvajal,[15] A. Celentano,[21] P. Chatagnon,[25] T. Chetry,[29] G. Ciullo,[19,14] L. Clark,[44] P.L. Cole,[28,18,9] M. Contalbrigo,[19] V. Crede,[16] R. Cruz-Torres,[1] A. D'Angelo,[22,36] N. Dashyan,[49] R. De Vita,[21] E. De Sanctis,[20] M. Defurne,[10] A. Deur,[40] S. Diehl,[11] C. Djalali,[33,38] M. Dugger,[5] R. Dupre,[25] H. Egiyan,[40] M. Ehrhart,[25] A. El Alaoui,[41] L. El Fassi,[29] P. Eugenio,[16] A. Filippi,[23] T.A. Forest,[18] G. Gavalian,[40,31] G.P. Gilfoyle,[35] K.L. Giovanetti,[26] F.X. Girod,[40] D.I. Glazier,[44] E. Golovatch,[37] R.W. Gothe,[38] K.A. Griffioen,[48] K. Hafidi,[51] H. Hakobyan,[41,49] N. Harrison,[40] M. Hattawy,[4] F. Hauenstein,[4] T.B. Hayward,[48] K. Hicks,[33] M. Holtrop,[31] Y. Ilieva,[38,17] I. Illari,[17] B.S. Ishkanov,[37] E.L. Isupov,[37] D. Jenkins,[46] H.S. Jo,[27] K. Joo,[11] M. Khachatryan,[4] A. Khanal,[15] M. Khandaker,[32,*] C.W. Kim,[17] W. Kim,[27] F.J. Klein,[9] V. Kubarovsky,[40,34] L. Lanza,[22] M. Leali,[43,24] P. Lenisa,[19] I.J.D. MacGregor,[44] D. Marchand,[25] N. Markov,[11] V. Mascagna,[42,24,†] B. McKinnon,[44] M. Mirazita,[20] V. Mokeev,[40] B. Mustafa,[51] S. Nanda,[29] S. Niccolai,[25] G. Niculescu,[26] M. Osipenko,[21] A.I. Ostrovidov,[16] M. Paolone,[39] L.L. Pappalardo,[19] R. Paremuzyan,[31] K. Park,[27,‡] E. Pasyuk,[40,5] W. Phelps,[17] O. Pogorelko,[30] J.W. Price,[6] Y. Prok,[4,47] D. Protopopescu,[44] M. Ripani,[21] D. Riser,[11] P. Rossi,[40,20] F. Sabatié,[10] R.A. Schumacher,[8] Y.G. Sharabian,[40] Iu. Skorodumina,[38,37] D. Sokhan,[44] O. Soto,[20] N. Sparveris,[39] S. Stepanyan,[40] I.I. Strakovsky,[17] S. Strauch,[38,17] N. Tyler,[38] M. Ungaro,[40,34] L. Venturelli,[43,24] H. Voskanyan,[49] E. Voutier,[25] R. Wang,[25] D.P. Watts,[45] X. Wei,[40] M.H. Wood,[7,38] N. Zachariou,[45] Z.W. Zhao,[12] and X. Zheng[52]

(The CLAS Collaboration)

[1]*Massachusetts Institute of Technology, Cambridge, MA 02139*

[2]*Hebrew University, Jerusalem, Israel*

[3]Tel Aviv University, Tel Aviv, Israel
[4]Old Dominion University, Norfolk, Virginia 23529
[5]Arizona State University, Tempe, Arizona 85287-1504
[6]California State University, Dominguez Hills, Carson, CA 90747
[7]Canisius College, Buffalo, NY
[8]Carnegie Mellon University, Pittsburgh, Pennsylvania 15213
[9]Catholic University of America, Washington, D.C. 20064
[10]IRFU, CEA, Universit'e Paris-Saclay, F-91191 Gif-sur-Yvette, France
[11]University of Connecticut, Storrs, Connecticut 06269
[12]Duke University, Durham, North Carolina 27708-0305
[13]Fairfield University, Fairfield CT 06824
[14]Universita' di Ferrara , 44121 Ferrara, Italy
[15]Florida International University, Miami, Florida 33199
[16]Florida State University, Tallahassee, Florida 32306
[17]The George Washington University, Washington, DC 20052
[18]Idaho State University, Pocatello, Idaho 83209
[19]INFN, Sezione di Ferrara, 44100 Ferrara, Italy
[20]INFN, Laboratori Nazionali di Frascati, 00044 Frascati, Italy
[21]INFN, Sezione di Genova, 16146 Genova, Italy
[22]INFN, Sezione di Roma Tor Vergata, 00133 Rome, Italy
[23]INFN, Sezione di Torino, 10125 Torino, Italy
[24]INFN, Sezione di Pavia, 27100 Pavia, Italy
[25]Institut de Physique Nucl'eaire, IN2P3-CNRS, Universit'e
Paris-Sud, Universit'e Paris-Saclay, F-91406 Orsay, France
[26]James Madison University, Harrisonburg, Virginia 22807
[27]Kyungpook National University, Daegu 41566, Republic of Korea
[28]Lamar University, 4400 MLK Blvd, PO Box 10009, Beaumont, Texas 77710
[29]Mississippi State University, Mississippi State, MS 39762-5167
[30]National Research Centre Kurchatov Institute - ITEP, Moscow, 117259, Russia
[31]University of New Hampshire, Durham, New Hampshire 03824-3568
[32]Norfolk State University, Norfolk, Virginia 23504
[33]Ohio University, Athens, Ohio 45701

[34]Rensselaer Polytechnic Institute, Troy, New York 12180-3590
[35]University of Richmond, Richmond, Virginia 23173
[36]Universita' di Roma Tor Vergata, 00133 Rome Italy
[37]Skobeltsyn Institute of Nuclear Physics, Lomonosov
Moscow State University, 119234 Moscow, Russia
[38]University of South Carolina, Columbia, South Carolina 29208
[39]Temple University, Philadelphia, PA 19122
[40]Thomas Jefferson National Accelerator Facility, Newport News, Virginia 23606
[41]Universidad Técnica Federico Santa María, Casilla 110-V Valparaíso, Chile
[42]Universita degli Studi dellInsubria, 22100 Como, Italy
[43]Universit'a degli Studi di Brescia, 25123 Brescia, Italy
[44]University of Glasgow, Glasgow G12 8QQ, United Kingdom
[45]University of York, York YO10 5DD, United Kingdom
[46]Virginia Tech, Blacksburg, Virginia 24061-0435
[47]University of Virginia, Charlottesville, Virginia 22901
[48]College of William and Mary, Williamsburg, Virginia 23187-8795
[49]Yerevan Physics Institute, 375036 Yerevan, Armenia
[50]Duquesne University, Pittsburgh, Pennsylvania. 15282 USA
[51]Argonne National Laboratory, Argonne, IL 60439
[52]University of Virginia, Charlottesville, VA 22901

(Dated: August 14, 2019)

Abstract

Abstract here

PACS numbers:

---

[*] Current address:Idaho State University, Pocatello, Idaho 83209

[†] Current address:Universit‘a degli Studi di Brescia, 25123 Brescia, Italy

[‡] Current address:Thomas Jefferson National Accelerator Facility, Newport News, Virginia 23606